ECAP-2012-026

Application of a time-resolving X-ray pixel detector in the detection of coincident fluorescence emissions after double K-shell vacancy production in the electron-capture decay of ^{55}Fe

Masterarbeit aus der Physik

Vorgelegt von
Benedikt Bergmann
10. September 2012

Erlangen Centre for Astroparticle Physics
Physikalisches Institut IV
Friedrich-Alexander-Universität Erlangen-Nürnberg

Betreuerin: Prof. Dr. Gisela Anton

Contents

1 Introduction

The process of photoionization, creating a single vacancy in an atomic shell, is a well known process. But due to electron correlation effects it may happen, that not only the photoelectron, but also another electron is liberated from the atom. If both are K-shell electrons, a so called "hollow atom" is created. These hollow atoms are also created in radioactive decays, where shake processes dominate the double K-shell vacancy production (This is described in more detail in section 2.1). The empty K-shell is then filled by electrons from higher shells emitting two fluorescence photons, that are shifted to higher energies than the usual diagram lines: the "hypersatellite" and "satellite" photon. The study of this hypersatellite line aroused the interest of many workers as it is an extremely sensitive probe of electron correlations within atoms, since double ionization would not occur in the absence of the electron-electron interaction [1]. It also provides information about relativistic effects (especially for medium-Z and heavier elements), the scheme of coupling (LS- or jj-coupling) or the Breit-Wigner interaction [2], [3]. The main problem hereby is that these hypersatellite lines are suppressed by about a factor of 10000 compared to the usual diagram lines.

The first observation of the hypersatellite satellite cascade following the electron capture decay of ^{55}Fe was performed by Charpak in 1953, who used two proportional counters in coincidence [1]. In 1973, Briand used a pair of germanium detectors and pointed out the energy shifts of the hypersatellites and the satellites from the normal diagram lines [4]. He also gave a value for the probability of the double K-shell related to the single vacancy production. Fast electron impact and ion-atom collisions are used to produce highly stripped atoms that result in complex spectra including hypersatellite and satellite lines.

In the experimental approach presented in this work the double K-vacancy production in the decay of a ^{55}Fe source was investigated using Timepix detectors in coincident measurements. The Timepix is a semiconductor hybrid pixel detector, that provides time as well as spatial information. Thus, these detectors have the capability of measuring a possible angular distribution between the hypersatellite and satellite momenta for the first time, which is shown in chapter 6.

Unfortunately, the Timepix is not able to provide time- and energy-information simultaneously. Nevertheless, the data evaluation for a high precision measurement of the

probability of the creation of a double K-shell compared to the single vacancy production is presented in chapter 3, solving the problem of not knowing the energies of the detected particles. The result obtained after 73 days of measuring is given in chapter 5.

2 Theoretical Background

Contents

2.1 Double K-shell vacancy production and hollow atoms

Hollow atoms, i.e. atoms with an empty K-shell, are produced either in radioactive decays or in photoelectric absorptions with a probability denoted P_{KK}, which is in the order of 10^{-5}-10^{-4}, depending on the atomic number Z with respect to the production of a single vacancy.

In the usual photoelectric absorption the incoming photon transfers its energy to a K-shell electron. If the energy of the incident photon is high enough, the second K-shell electron can also be emitted. This effect is mainly due to the electron-electron scattering, called knock-out (KO) that dominates at lower incident photon energies, and the shake-processes (SSO), where a fast photoelectron leaves with most of the energy and the second electron is shaken-up or -off due to the relaxation of the excited atom. This also leads to the concept of an energy independent asymptotic limit of the ratio between double and single K-shell vacancy production [1]. The energy dependence of these effects for silver can be seen in figure 2.1.

A good tool for the investigation of asymptotic limits are electron capture decays. In this, one of the electrons is absorbed in the nucleus and consequently there is only one electron and the empty K-shell states. The double K-shell vacancy production proceeds only by a shake-off process.

Now, the double to single K-shell vacancy production does not solely depend on the energy of the EC/photo-electron (which depends on the incident photon energy in case of photoionization) but also on the element used. P_{KK} as a function of the atomic number

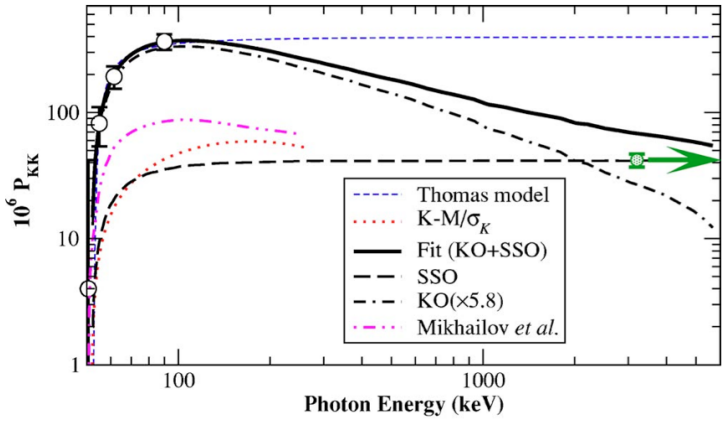

Figure 2.1 Energy dependence of P_{KK} for silver. The value for the asymptotic limit is given by the green arrow [1].

can be modeled as a power-law, i.e. $P_{\mathrm{KK}} \propto Z^{-1.61}$ (solid line in figure 2.2).

As next let's have a closer look at the decay scheme of hollow atoms. As there are two vacancies in the K-shell that have to be filled, this can be seen as a two step process:

1. The first K-vacancy is filled by an electron from a higher shell. With a given probability, which is called the fluorescence yield ω_{K}, a fluorescence photon is emitted. The energy of this fluorescence photon is shifted to higher energies as the Coulomb-potential is less shielded due to the empty K-shell. It is called "hypersatellite".

2. Now there is still one vacancy left in the K-shell plus an additional spectator vacancy in a higher shell. Again the remaining hole in the K-shell is filled by an electron from a higher shell. With the probability ω_{K}, another fluorescence photon, which is referred to as "satellite", is emitted. This one again is shifted to higher energies because the spectator vacancy reduces the shielding. It is assumed that the fluorescence yields are the same for the satellites and hypersatellites: $\omega_{\mathrm{K}}^{\mathrm{satellite}} = \omega_{\mathrm{K}}^{\mathrm{hypersatellite}}$.

These energy shifts are illustrated for manganese in figure 2.3. It is the hollow atom that is investigated in this work. $\mathrm{K}_{\alpha}^{\mathrm{h}}$ denotes the K_{α}-hypersatellite and $\mathrm{K}_{\alpha}\mathrm{L}^1$ the K_{α}-satellite with one spectator vacancy in the L-shell.

The P_{KK}-values are theoretically calculated using the so called sudden approximation. The theoretical results are summarized in figure 2.4. As one can see the calculated values strongly depend on the method that is used for their calculation.

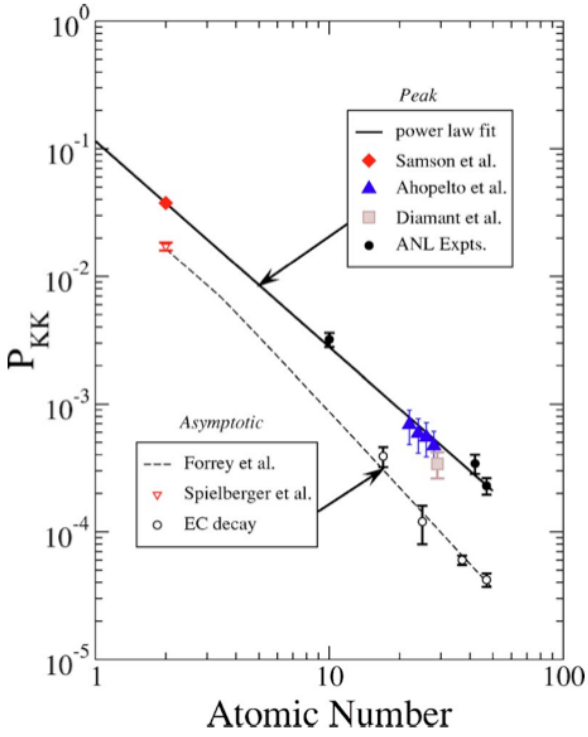

Figure 2.2 Z-dependence of the P_{KK} value [1].

Various experiments were performed to measure this value. These range from spectroscopic measurements to coincident measurements. The result with the lowest uncertainty is given as $P_{\mathrm{KK}} = (1.3 \pm 0.2) \cdot 10^{-4}$ [5] in 1991 and shows only moderate improvement to the first one obtained by Briand in 1973: $P_{\mathrm{KK}} = (1.2 \pm 0.4) \cdot 10^{-4}$ [4].

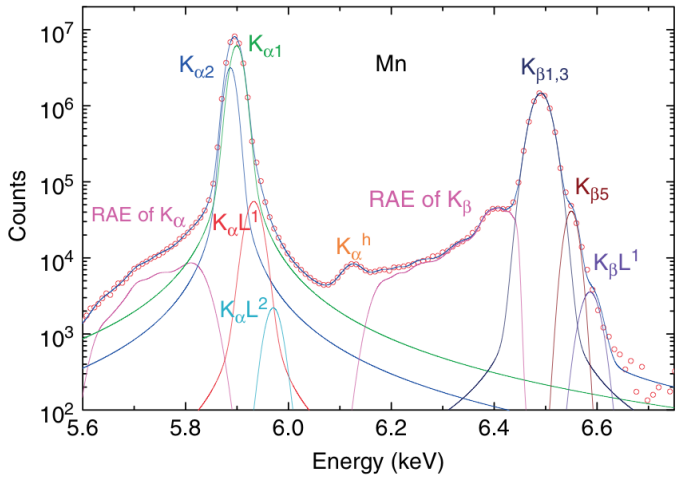

Figure 2.3 Energy spectrum of the manganese fluorescence lines obtained with an X-Ray spectrometer. RAE means Radiative Auger Effect, i.e. electrons are emitted instead of fluorescence photons [2].

P_{KK}	Method
4.8×10^{-4}	Correlation effects neglected
0.881×10^{-4}	Initial state correlation by screening constant
1.13×10^{-4}	Coulomb propagator method
2.4×10^{-4}	SCF potential plus final-state correlation
0.904×10^{-4}	Correlation-split wave function

Figure 2.4 Table of theoretical P_{KK}-values for ^{55}Fe using different methods [5].

2.2 Electron Capture Decay of ^{55}Fe

During an electron capture an electron from an atomic shell is absorbed by a proton rich nucleus, wherefore a proton is changed into a neutron by interacting with this electron. A neutrino is emitted and the atom is left with a hole in the atomic shell. This can be written as

$$\mathrm{p}^+ + \mathrm{e}^- \rightarrow \mathrm{n} + \nu_{\mathrm{e}^-}. \tag{2.1}$$

If the proton is embedded in a nucleus, this can be expressed as

$$^{\mathrm{A}}_{\mathrm{Z}}\mathrm{X} + \mathrm{e}^- \rightarrow {}_{\mathrm{Z}-1}{}^{\mathrm{A}}\mathrm{Y} + \nu_{\mathrm{e}^-}, \tag{2.2}$$

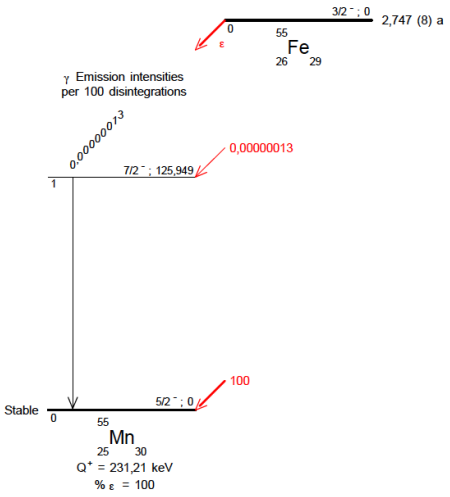

Figure 2.5 Nuclear decay scheme of Fe55 [6].

where a nucleus X with mass number A, and atomic number Z decays into a nucleus Y with the same mass number and atomic number Z-1.

The decay of ^{55}Fe, which is the source used throughout this work has a Q-value of 231.21 keV (The Q-value is the energy difference of final and initial state) and a half-life time of $T_{1/2} = 2.747$ a to the stable ground state of the manganese (see figure 2.5). With a negligible probability of $1.3 \cdot 10^{-7}$% a gamma emission at an energy of 105.26 keV is observed [6].

As this decay leads to an atom with one inner-shell vacancy, the electron capture process is followed by the emission of X-rays. The probabilities of these fluorescence lines per 100 disintegrations are given in table 2.1.

Fluorescence Line	Energy in keV	Probability per 100 disintegrations
K_{α_1}	5.899	16.9
K_{α_2}	5.888	8.5
K_{α_2}	5.77	0.0000069
K_{β_1}	6.49	1.98
K_{β_3}	6.49	1.01
K_{β_4}	6.539	0.000000085
K_{β_5}	6.536	0.00089
L	0.556 - 0.721	0.524

Table 2.1 Energies and probabilities of the X-Ray emissions following an electron capture decay of ^{55}Fe. Values taken from [6].

2.3 Timepix detectors

The Timepix detectors are semiconductor pixelated X-ray imaging detectors, that were developed in the Medipix-Collaboration together with CERN and EUDET. Based on the technology of the Medipix2, the Timepix device can provide arrival time information in the time of arrival mode (ToA), energy information in the time over threshold mode (ToT) and pure event counting information in the Medipix mode.

Figure 2.6 (a) shows a Timepix detector with an USB readout. The sensor layer (A), the chipboard with the electronics (C) and readout (D) can be seen.

In the sensor layer (A) the actual interaction with the particle that should be detected takes place. Depending on the application silicon or other semiconductors, like cadmium telluride (CdTe) can be chosen as a sensor material. The dimensions of this layer are usually 1.4 cm times 1.4 cm, where the thickness ranges from 0.3 mm up to 1 mm. In this work a silicon sensor with a thickness of 0.3 mm was used.

This semiconductor layer is connected via bump bonds to the pixelated electronical part, the ASIC. This can be seen in figure 2.6 (b). The pixel pitch, which is the size of the electrodes, is 55 μm, thus the sensor layer is divided into 256 times 256 single pixels.

The chipboard, containing the electronics, is needed for the power supply of the ASIC as well as the data transfer from and to the readout (D), which extracts the data from the detector.

The detection process can be described as follows: An incoming photon interacts in the sensor layer so that a photoelectron is created. On its way through the layer this photoelectron creates electron-hole pairs. The number of the produced pairs is

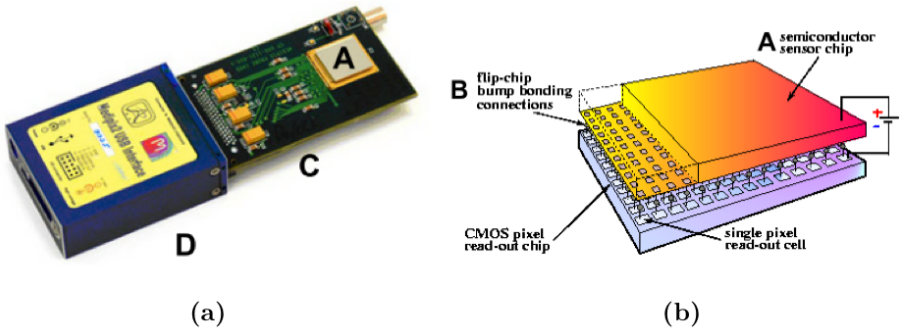

(a) (b)

Figure 2.6 Picture of a Timepix detector with a USB-readout (a) and the scheme of the bump bonded sensor layer (b). A indicates the sensor layer, B the bump bonds with the pixelated ASIC, C the chipboard that contains the electronics and D the USB-readout [7].

proportional to the energy of the photoelectron and also proportional to the energy of the incident photon. Due to an applied electrical field this charge carriers drift either to the top of the sensor layer or to the pixel electronics and induce charge at the pixel electrodes. In the analogue part of the pixel electronics (see fig. 2.7) a charge sensitive amplifier (CSA) generates a voltage pulse, with a height proportional to the charge collected in the pixel, that is shaped with a pulse shaper and compared with a given, adjustable threshold (THL) in a discriminator. If the pulse is high enough, the counter is incremented depending on the adjusted mode.

In order to illustrate the different modes the shaped voltage pulse generated in the preamplifier is shown in figures 2.8 and 2.9. In the different modes this signal is used in different ways:

- In the counting or Medipix mode each time the pulse exceeds the threshold level (THL) in the given acquisition time a counter is incremented by one, so one gets the information how often a pixel has been hit in one frame.
- In the ToA mode the time is measured from the first time the pulse is over the THL to the end of the frame. This is realized by counting the clock pulses of a reference clock (see figure 2.8).
- The ToT mode then measures in a similar way the time that the signal is above the THL-level and provides energy information (see figure 2.9). More details on this mode and the calibration procedure can be found in [7], section III.3.

The digital to analogue converter (DAC) converts the digital detector settings for the measurement, like THL and PreAmp, adjusted by the user into analogue signals. There

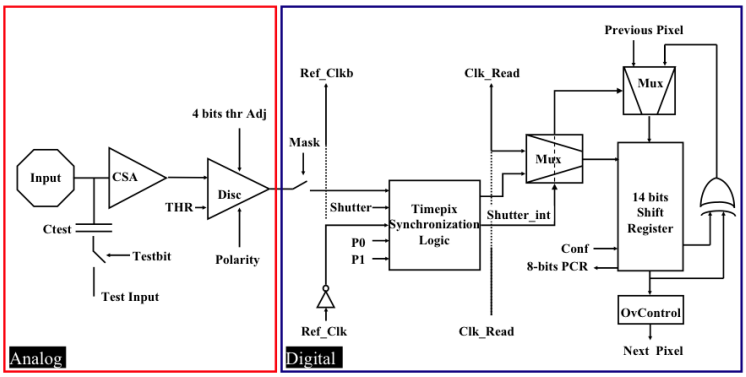

Figure 2.7 Scheme of the analogue and digital part of the Timepix pixel cell [8].

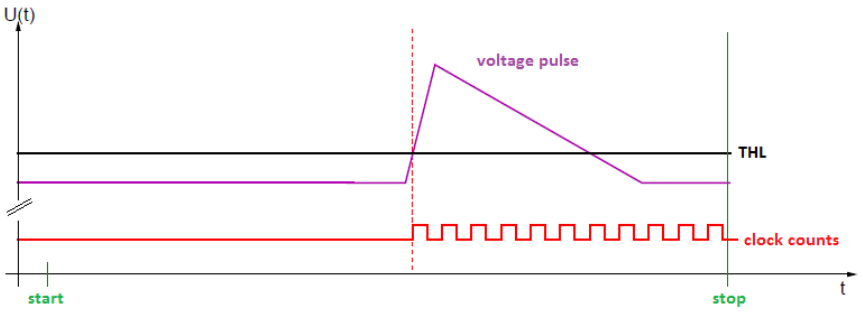

Figure 2.8 In ToA mode the time is measured in clock counts from the first time the voltage pulse generated in the preamplifier is above the threshold level (THL) to the end of the frame. According [9].

are several values that can be set. The important ones for measurements in the ToA mode are THL and PreAmp. The PreAmp value determines the gain of the preamplifier signal, thus a high PreAmp leads to steep pulses. The effect of the PreAmp value is demonstrated in figure 2.10. As we are interested in a fast response to the events, this value is set to the maximum.

The time between the clock pulses is $\Delta T = \frac{1}{f_{\text{clock}}}$. As in this work always the highest available clock $f_{\text{clock}} = 48\,\text{MHz}$ was adjusted one finds $\Delta T = 20.8\,\text{ns}$. This is the minimal time difference between two detected events. The timing resolution is worse because of the time walk effect, that is due to the different times the voltage pulses with different heights cross the THL level, as the rising times are always about 100 ns to 150 ns [10], section 3.2.3, [8] chapter 5 (see figure 2.11).

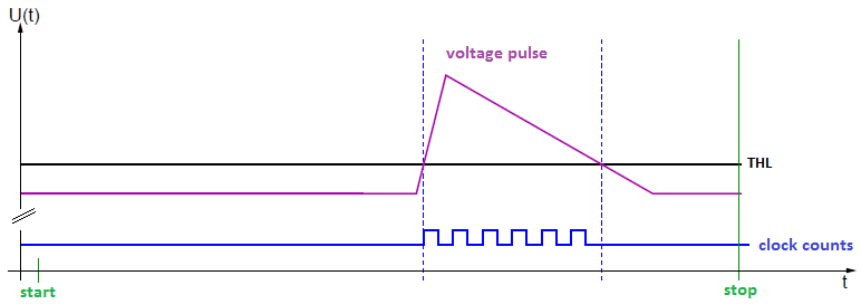

Figure 2.9 In ToT mode the time is measured in clock counts when the voltage pulse generated in the preamplifier is above the threshold level (THL). According [9].

Due to the pixelisation of the detector, charge sharing can occur. Here the charge cloud of one photon event is broadened due to diffusion and repulsion so that a single photon deposits energy in more than one pixel. For further information on this see also [11] or [12].

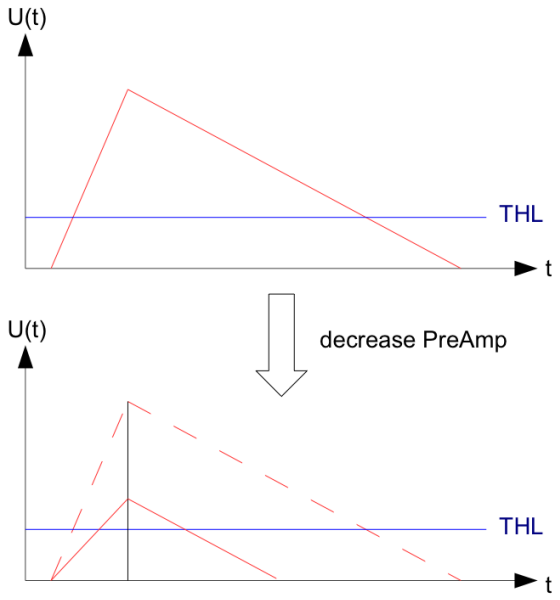

Figure 2.10 The PreAmp value determines the steepness of the pulse. A low PreAmp value generates flat-angle pulses, high values steep ones.

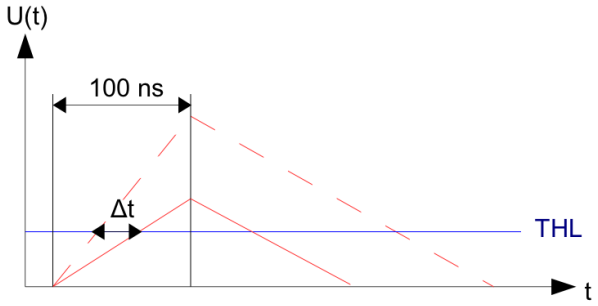

Figure 2.11 Illustration of the time walk effect. As the rising time is given to be the same for all energies deposited in the pixel, but the pulse height differs with this energy, a time delay Δt can occur between two coincident events.

2.4 FitPix-Readout and Pixelman software

For the communication between detector and computer the FitPix readout was used. It provides reference clock frequencies up to 48 MHz and readout speeds up to 90 frames per second, when burst mode is activated, and bias voltages between 5 V and 100 V. For the presented work the maximum available clock frequency of 48 MHz was used. As the maximum counter value of each pixel is 11810, the frametime in ToA-mode is correlated to this frequency and one finds the maximum frametime to be $t_{\text{frame}} = \frac{11810}{f_{\text{clock}}}$. Further information on the readout can be found on [13].

This interface is connected to the PC via USB 2.0 and can be controlled by the Pixelman software (see [14]). Details on the readout and software will be described when they are needed.

2.5 Monte-Carlo simulation package ROSI

To simulate the different geometries and detector responses the Monte-Carlo simulation package ROSI (ROentgen SImulation) is used. The physics of interaction in ROSI is based on the packages EGS4 and its expansion LSCAT. Random variables are generated with RAVAR. A complete documentation with examples can be found in [15].

For the simulation of the response of a Timepix-device ROSI applications, developed at the physical institute of Erlangen, are used, where the detector response is adapted to pixelated photon counting detectors. Details on this versions can be found in [11] and [12].

3 Plan for the measurements and details on the evaluation

In this work a ^{55}Fe source was used for a time of arrival coincidence measurement on the hypersatellite-satellite emission. The choice of the source has various reasons:

1. The predicted P_{KK}-value is in the order of 10^{-4} (see section 2.1), which is high compared to elements with higher atomic numbers.
2. The experimental data available up to now does not prefer one calculated value as the errors are too large (see section 2.1).
3. The detection efficiency of the silicon detector for the fluorescence photons of the manganese atom is high (see chapter 4.3).
4. It is a "clean"-source, meaning there are no additional γ-lines from excited states of the core. This is a hard criterion because the measurements are performed in the time of arrival mode, wherefore no energy information can be used to distinguish between these contributions.

For measurements of the P_{KK}-value frames were taken in the ToA-mode. Thus, one gets the information which pixel was hit at what time. In the evaluation of this ToA-data only those frames were taken, that contain exactly two clusters with multiplicities one or two, as due to charge sharing one photon can also trigger two pixel. Examples of these clusters are illustrated in figure 3.1. The cut on the cluster sizes is done to get rid of cosmic myons that show longer tracks on the pixel matrix (see [7], sections II.3.2 and IV).

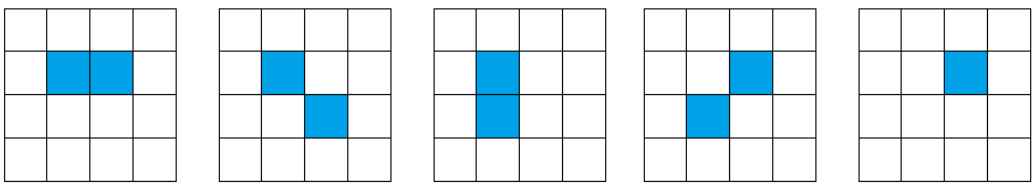

Figure 3.1 Illustration of clusters with multiplicities one or two.

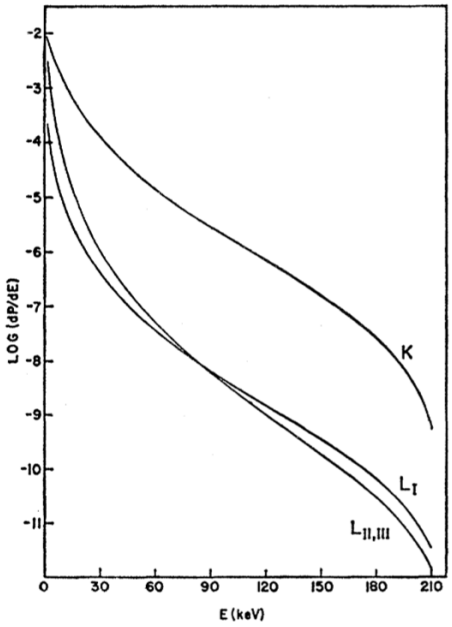

Figure 3.2 Energy spectrum of the emission of electrons in coincidence with K-X-rays. The electron spectrum is theoretically predicted by Primakoff and Porter. The lower two curves are shake-off electrons from higher shells and are backgroiund events. The upper curve, the shake-off electrons from the K-shell contribute to the signal and the background [16].

As usual, there are background events that cannot be avoided completely. First, there are random coincidences from two separate fluorescence photons emitted from different atoms. As will be shown in section 4.5 this can easily be coped with a fit to the spectrum of time differences. The two main background sources are the Internal Bremsstrahlung (IB) photons and the shake-off electrons, which are also coincident with K-X-rays (see [16] and [17]). Figures 3.2 and 3.3 show the energy spectra of these background contributions.

Consequently, one has to do some calculations on how often an event, meaning two clusters with multiplicities one or two in one frame, can occur. As already mentioned in chapter 2.1, in electron captures the main process for the creation of a hollow atom is the shake-off process. This leads to the emission of an electron and leaves the atom with two vacancies in the K-shell. The measured rate for these events $R_{\mathrm{KK}}^{\mathrm{meas}}$ can then be expressed as

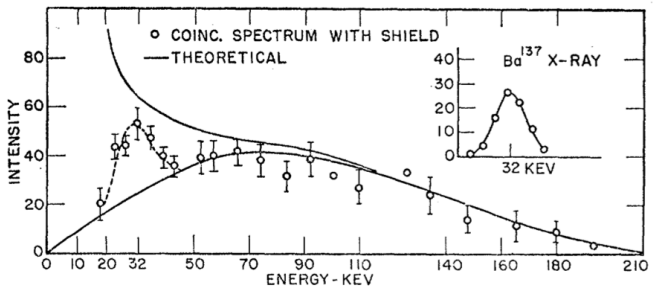

Figure 3.3 Energy spectrum of the coincident IB emission, theoretically predicted (lower solid curve) and measured. The upper solid curve is the theoretical prediction for the total IB spectrum [17].

$$R_{\mathrm{KK}}^{\mathrm{meas}} = P_{\mathrm{KK}} \cdot [\underbrace{\delta_\gamma^{\mathrm{HS}} \delta_\gamma (1-\delta_{\text{e-}}) \omega_{K_{\alpha,\beta}}^2}_{\gamma_{\mathrm{HS}},\gamma,\overline{\text{e-}}} + \underbrace{(1-\delta_\gamma^{\mathrm{HS}}) \delta_\gamma \delta_{\text{e-}} \omega_{K_{\alpha,\beta}}^2}_{\overline{\gamma_{\mathrm{HS}}},\gamma,\text{e-}} + \underbrace{\delta_\gamma^{\mathrm{HS}} (1-\delta_\gamma) \delta_{\text{e-}} \omega_{K_{\alpha,\beta}}^2}_{\gamma_{\mathrm{HS}},\overline{\gamma},\text{e-}}}_{\gamma_{\mathrm{HS}},(1-\gamma),\text{e-}} + \underbrace{\delta_\gamma^{\mathrm{HS}} \delta_{\text{e-}} \omega_{K_{\alpha,\beta}} (1-\omega_{K_{\alpha,\beta}})}_{\gamma_{\mathrm{HS}},(1-\gamma),\text{e-}} + \underbrace{\delta_\gamma \delta_{\text{e-}} \omega_{K_{\alpha,\beta}} (1-\omega_{K_{\alpha,\beta}})}_{(1-\gamma_{\mathrm{HS}}),\gamma,\text{e-}}] \cdot A_{\mathrm{source}}, \tag{3.1}$$

where P_{KK} is the probability of the shake-off process, A_{source} is the activity of the iron source, $\omega_{K_{\alpha,\beta}}$ is the fluorescence yield for the emission of K_α- or K_β-fluorescence photons and δ_{i} is the probability that an emitted particle i from the source is used for the evaluation. These "detection yields" δ_{i} can be seen as the product of the solid angle-acceptance, the detection efficiency and the probability that the considered particle produces a cluster with multiplicities one or two, $\delta_{\mathrm{i}} = \epsilon_{\mathrm{SA}} \cdot \epsilon_{\mathrm{detection}} \cdot P_{\mathrm{cluster<3}}$. Three assumptions are made in this formula:

1. The fluorescence yields for the single $\omega_{K_{\alpha,\beta}}$ and the double K-shell vacancy $\omega_{KK_{\alpha,\beta}}$ configuration are the same, i.e. $\omega_{K_{\alpha,\beta}} = \omega_{KK_{\alpha,\beta}}$. The difference of this two values was reported to be less than 6% (see [1]).

2. All particles are emitted independently and isotropically: There is no angular dependence between any possible measured coincidence. Thus, the detection yields can be calculated separately and multiplied. In chapter 6 an attempt is presented to prove this assumption.

3. As the energy shifts of the K-satellites are small, their detection yield is the same as the one for the K diagram line photons: $\delta_\gamma^{\mathrm{satellite}} = \delta_\gamma$.

In the following there is a short description of the terms of equation 3.1:

- $\gamma_{\mathrm{HS}}, \gamma, \overline{\text{e-}}$: Two fluorescence photons and the electron are emitted, where the two photons are measured and the electron is not detected. The first emitted photon is the hypersatellite, and shifted to higher energies and the second one a satellite, which has approximately the energy of the normal fluorescence line. The values for the energy-shifts of the K_α and K_β-hypersatellites can be found in [4].

- $\overline{\gamma_{\mathrm{HS}}}, \gamma$, e- and $\gamma_{\mathrm{HS}}, \overline{\gamma}$, e-: These again stand for the coincident hypersatellite satellite emission but here either the hypersatellite or the satellite photon is not seen but the electron is detected.

- $\gamma_{\mathrm{HS}}, (1-\gamma)$, e- and $(1-\gamma_{\mathrm{HS}}), \gamma$, e-: Here just one photon, either the hypersatellite or the satellite, is emitted, and the other K-shell vacancy is filled while a low energy Auger-electron is emitted, that can not be detected.

The rate of the background $R_{\mathrm{BG}}^{\mathrm{meas}}$ can then be calculated as

$$R_{\mathrm{BG}}^{\mathrm{meas}} = (P_{\text{e-}}\delta_\gamma\delta_{\text{e-}}\omega_{K_{\alpha,\beta}} + P_{\mathrm{IB}}\delta_\gamma\delta_{IB}\omega_{K_{\alpha,\beta}})) \cdot A_{\mathrm{source}}, \tag{3.2}$$

where P_{IB} and $P_{\text{e-}}$ are the probabilities for the emission of Internal Bremsstrahlung-photons and L- or M-shell shake-off electrons after the K-electron capture as well as K-shake-off electrons after L- (or M-) electron capture, respectively. Figure 3.4 illustrates the processes leading to signal and background events.

The measured rate $R_{\mathrm{DL}}^{\mathrm{meas}}$ of the usual K diagram line photons can be expressed as

$$R_{\mathrm{DL}}^{\mathrm{meas}} = \delta_\gamma \cdot \omega_{K_{\alpha,\beta}} \cdot A_{\mathrm{source}}. \tag{3.3}$$

Using this relation and combining equations 3.1 and 3.2 one finds

$$R_{\mathrm{coinc}}^{\mathrm{meas}} = [P_{\mathrm{KK}}(\delta_\gamma^{\mathrm{HS}}\omega_{K_{\alpha,\beta}} - 3\cdot\delta_\gamma^{\mathrm{HS}}\delta_{\text{e-}}\omega_{K_{\alpha,\beta}} + \delta_{\text{e-}}(1+\frac{\delta_\gamma^{\mathrm{HS}}}{\delta_\gamma})) + \delta_{\text{e-}}P_{\text{e-}} + \delta_{\mathrm{IB}}P_{\mathrm{IB}}]\cdot R_{\mathrm{DL}}^{\mathrm{meas}}. \tag{3.4}$$

As these rates are measured simultaneously, the measuring time is the same and equation 3.4 can be written as

$$N_{\mathrm{coinc}}^{\mathrm{meas}} = [P_{\mathrm{KK}}(\delta_\gamma^{\mathrm{HS}}\omega_{K_{\alpha,\beta}} - 3\cdot\delta_\gamma^{\mathrm{HS}}\delta_{\text{e-}}\omega_{K_{\alpha,\beta}} + \delta_{\text{e-}}(1+\frac{\delta_\gamma^{\mathrm{HS}}}{\delta_\gamma})) + \delta_{\text{e-}}P_{\text{e-}} + \delta_{\mathrm{IB}}P_{\mathrm{IB}}]\cdot N_{\mathrm{DL}}^{\mathrm{measured}}. \tag{3.5}$$

This formula links different types of variables: The quantities taken from the measurement $N_{\mathrm{coinc}}^{\mathrm{meas}}$ and $N_{\mathrm{DL}}^{\mathrm{meas}}$, the detection yields δ_{i}, that have to be simulated, the probabilities P_{IB}, $P_{\text{e-}}$ and finally the parameter P_{KK} that should be determined. Although the absolute value of the emission of an Internal Bremsstrahlung photon is given

to be $P_{\mathrm{IB}} = (3.24 \pm 0.06) \cdot 10^{-5}$ [6], there are still two unknown values: P_{KK} (that is the subject of this investigation) and $P_{\text{e-}}$.

To cope with this problem of two unknown parameters a second measurement is performed: A thin Kapton-foil was inserted between the source and the sensor layer to decrease the number of electrons impinging on the detector. This foil also changes the detection yields for the low energy fluorescence photons emitted from the source (these detection yields are then labeled "Kapton"), where it has nearly no effect on the detection yields for the high energy Internal Bremsstrahlung photons, i.e. $\delta_{\mathrm{IB}}^{\mathrm{Kapton}} = \delta_{\mathrm{IB}}$. Now a second equation is found and one obtains a linear system of two equations for two unknown variables:

$$\begin{aligned} N_{\mathrm{coin}}^{\mathrm{meas}} =& [P_{\mathrm{KK}} \overbrace{(\delta_\gamma^{\mathrm{HS}} \omega_{K_{\alpha,\beta}} - 3 \cdot \delta_\gamma^{\mathrm{HS}} \delta_{\text{e-}} \omega_{K_{\alpha,\beta}} + \delta_{\text{e-}}(1 + \frac{\delta_\gamma^{\mathrm{HS}}}{\delta_\gamma}))}^{=:\alpha_\gamma} + \delta_{\text{e-}} P_{\text{e-}} + \delta_{\mathrm{IB}} P_{\mathrm{IB}}] \cdot N_{\mathrm{DL}}^{\mathrm{meas}} \\ N_{\mathrm{coin}}^{\mathrm{meas,Kapton}} =& [P_{\mathrm{KK}} \overbrace{(\delta_\gamma^{\mathrm{HS,Kapton}} \omega_{K_{\alpha,\beta}} - 3 \cdot \delta_\gamma^{\mathrm{HS,Kapton}} \delta_{\text{e-}}^{\mathrm{Kapton}} \omega_{K_{\alpha,\beta}} + \delta_{\text{e-}}^{\mathrm{Kapton}}(1 + \frac{\delta_\gamma^{\mathrm{HS,Kapton}}}{\delta_\gamma^{\mathrm{Kapton}}}))}^{=:\alpha_\gamma^{\mathrm{Kapton}}} \\ & + \delta_{\text{e-}}^{\mathrm{Kapton}} P_{\text{e-}} + \delta_{\mathrm{IB}} P_{\mathrm{IB}}] \cdot N_{\mathrm{DL}}^{\mathrm{meas,Kapton}} \end{aligned} \tag{3.6}$$

So that now P_{KK} is given by the formula

$$P_{\mathrm{KK}} = \frac{\frac{N_{\mathrm{coinc}}^{\mathrm{meas,Kapton}}}{N_{\mathrm{DL}}^{\mathrm{Kapton}}} - \frac{\delta_{\text{e-}}^{\mathrm{Kapton}} N_{\mathrm{coinc}}^{\mathrm{meas}}}{\delta_{\text{e-}} N_{\mathrm{DL}}} - \delta_{\mathrm{IB}} P_{\mathrm{IB}} (1 - \frac{\delta_{\text{e-}}^{\mathrm{Kapton}}}{\delta_{\text{e-}}})}{\alpha_\gamma - \alpha_\gamma^{\mathrm{Kapton}} \cdot \frac{\delta_{\text{e-}}^{\mathrm{Kapton}}}{\delta_{\text{e-}}}}, \tag{3.7}$$

where the abbreviations α_γ and $\alpha_\gamma^{\mathrm{Kapton}}$ are introduced to simplify the expression.

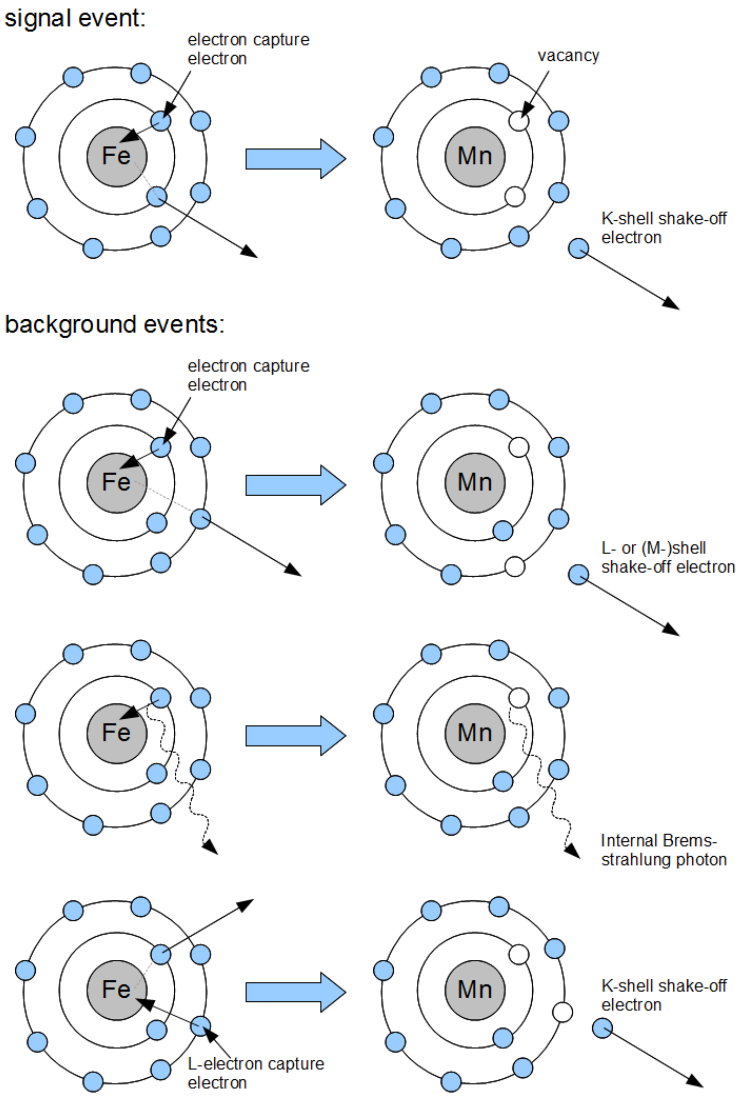

Figure 3.4 Illustration of the creation of a double K-shell vacancy (signal event) and background events: Due to coincidences of Internal Bremsstrahlung photons or L- or M-shell shake-off electrons with K-X-rays and due to K-shell shake-off electrons and K-X-rays after L- (or M-)electron capture.

4 Measurements on the performance of the detector and simulation results

Contents

In the previous section the plan for the evaluation of the measurement of the P_{KK}-values was described. Before this can be done, the detection yields have to be simulated. For modeling the response of the Timepix-devices the ROSI-simulation needs the information what is the lowest energy that can be detected. To get this energetic quantity (in keV) first a THL-Scan has to be performed (see section 4.2). The detectors are described in section 4.1. The next step is to prove, if the simulation gives the correct detection efficiencies (see 4.3). As this is the case, a fine tuning of the geometry can be done in order to reproduce the measured detection yields.

In section 4.5 the complete evaluation is performed for data measured with a single detector in a one sided stack.

4.1 Detectors

The two detectors used are H09W15, a class B detector with one dead column, and I02W15, a class A detector. The THL-adjustments for the chips have already been done by Michael Böhnel (H09W15) and Ferdinand Lück (I02W15) [18]. The loaded masks are shown in figure 4.1, the DAC-settings for the measurements in table 4.1. The bias voltage U_{bias}

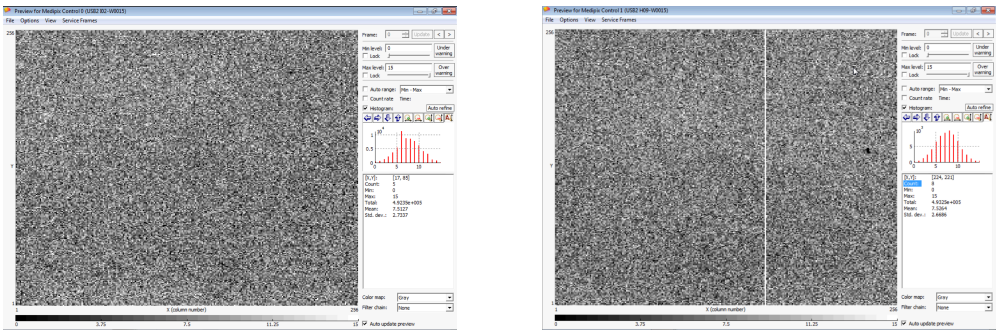

Figure 4.1 Loaded masks for the two detectors used in this work: I02W15, a class A detector, on the left, and H09W15, a class B detector with one dead column, on the right.

is set to 100 V. If the values are changed, this will be described in the appropriate chapter.

DAC	I02W15	H09W15
IKrum	5	5
Disc	127	127
Preamp	255	255
BuffAnalogA	127	127
BuffAnalogB	127	127
Hist	0	0
THL	430	930
THLCoarse	7	6
Vcas	130	130
FBK	128	135
GND	80	80
THS	73	67
BiasLVDS	128	128
RefLVDS	128	128

Table 4.1 DAC-settings for the performed measurements.

4.2 THL-Scans

The first step is to perform a THL-scan for the two detectors to determine the lowest energy that can be measured. This information is an important input for the simulation. Therefore the detector is illuminated with photons of different, but known energies, which is achieved by placing the ^{55}Fe-source in front of the detector or by using different foils (Pb and Sn) as X-ray fluorescence targets (see figure 4.2). The counting mode of the detectors is used.

The THL-scan proceeds as follows:

1. The source is placed in front of the sensor layer, or the X-ray tube is switched on.
2. A low THL value (corresponding to a high energetic threshold level) is set in the pixelman software, so that nearly no pixel is counting.
3. The actual THL scan is started. After each frame the THL-value is increased (i.e. the threshold energy decreased) by one and the hits on the pixel matrix are counted. When the THL-level falls below the energy of a fluorescence line of the X-ray source, the measured counts increase rapidly. An integrated spectrum is obtained. If the derivative of this spectrum is plotted, one will find peaks at the THL-values corresponding to the fluorescence energies of the target (or the source).

For the evaluation a ROOT-script [19] was written, where the counts on the whole matrix for each THL were filled into a histogram and then the derivative is calculated as the

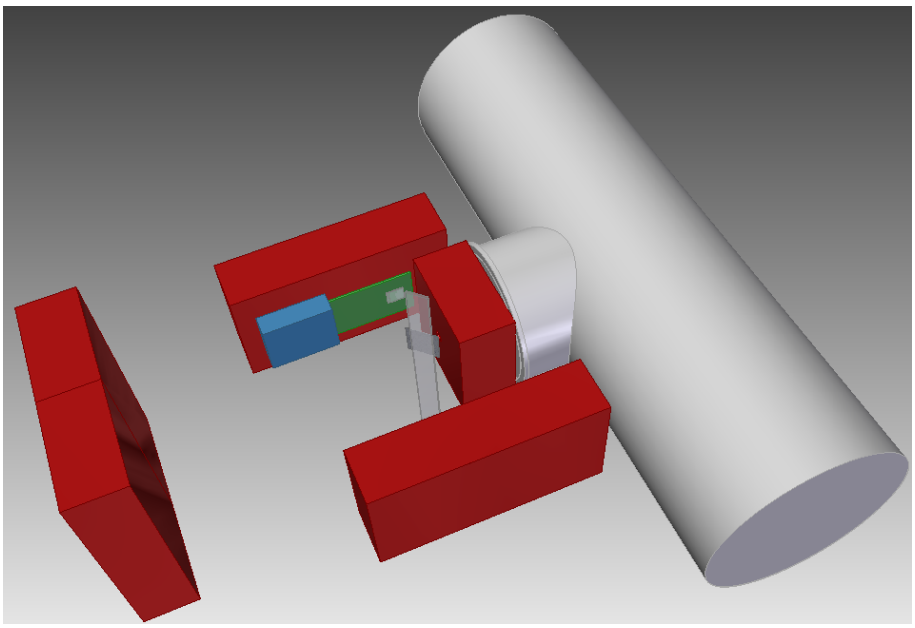

Figure 4.2 Setup for the THL-scans. The X-ray tube illuminates the foil, so that holes in the atomic shell are created that are filled with electrons from higher shells and the characteristic fluorescence lines are measured. Drawing by Peter Sievers.

difference of the contents of two neighboring bins, $h_{\mathrm{i}+1}$ and h_{i}, divided by the difference of the THL values of these bins:

$$\frac{d\mathrm{Counts}}{d\mathrm{THL}} = \frac{h_{\mathrm{i}+1} - h_{\mathrm{i}}}{\mathrm{THL}_{\mathrm{i}+1} - \mathrm{THL}_{\mathrm{i}}}. \tag{4.1}$$

The spectra obtained for the two detectors are shown in figures 4.3 and 4.4.

The peaks, that can be seen in these plots, correspond to the energy deposited in the detector by the fluorescence photons. To determine the peak positions, the responses of the detector to the different characteristic X-ray spectra have to be simulated. The data for the X-ray spectra are taken from [20]. To the measured as well as the simulated spectra the gaussian distributions $\frac{d\mathrm{Counts}}{d\mathrm{THL}}(x) = A \cdot e^{-\frac{x-\mathrm{THL}_{\mathrm{mean}}}{2\cdot\sigma^2_{\mathrm{THL}}}}$ and $\frac{d\mathrm{Counts}}{d\mathrm{E}}(x) = A \cdot e^{-\frac{x-E_{\mathrm{mean}}}{2\cdot\sigma^2_{\mathrm{E}}}}$ are fitted. The parameters of the fit used for the further evaluation are given in table 4.2.

The calibration curve can easily be obtained by plotting the simulated energies E_{mean} versus $\mathrm{THL}_{\mathrm{mean}}$ and doing a linear fit $E(\mathrm{THL}) = m \cdot \mathrm{THL} + t$ to this data (see figures 4.5 and 4.6), and one finds

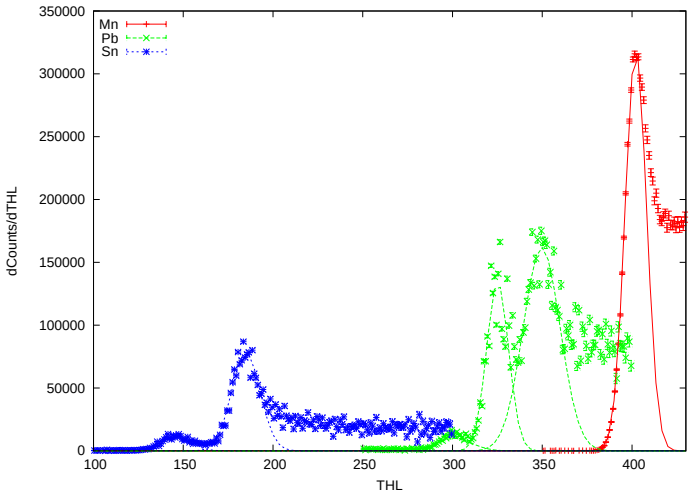

Figure 4.3 Measured THL spectra with the gaussian fits to the peaks (detector I02W15).

$$\begin{aligned} E_{\mathrm{I02W15}}(\mathrm{THL}) &= -\underbrace{0.0889588}_{\pm 0.0001749}\ \mathrm{keV}\cdot\mathrm{THL} + \underbrace{41.3972}_{\pm 0.06812}\ \mathrm{keV} \\ E_{\mathrm{H09W15}}(\mathrm{THL}) &= -\underbrace{0.0900285}_{\pm 0.0002594}\ \mathrm{keV}\cdot\mathrm{THL} + \underbrace{86.9877}_{\pm 0.2281}\ \mathrm{keV}. \end{aligned} \tag{4.2}$$

By using this calibration curves the differentiated spectra are plotted versus the energy deposited in the detector (see figures 4.7 and 4.8).

The adjusted threshold levels (see section 4.1) are chosen to be just above the noise level of the detectors and can be assigned to the energy values $E^{\mathrm{I02W15}}_{\mathrm{THL}=430} = (3.145 \pm 0.101)\,\mathrm{keV}$ and $E^{\mathrm{H09W15}}_{\mathrm{THL}=930} = (3.261 \pm 0.332)\,\mathrm{keV}$, where the errors are given by $\Delta E(\mathrm{THL}) = \sqrt{(\mathrm{THL}\cdot\Delta m)^2 + (\Delta t)^2}$.

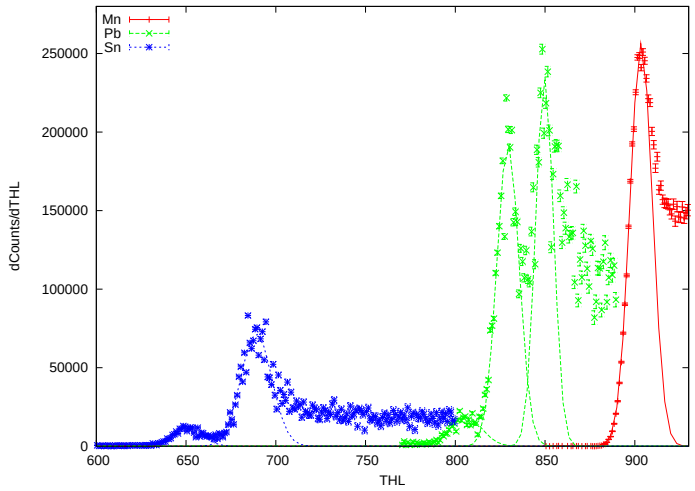

Figure 4.4 Measured THL spectra with the gaussian fits to the peaks (detector H09W15).

Element	Energy E_{mean} in keV	$\text{THL}_{\text{mean}}^{\text{I02W15}}$	$\text{THL}_{\text{mean}}^{\text{H09W15}}$
Mn	5.635 ± 0.003	402.13 ± 0.06	903.72 ± 0.10
Pb	10.338 ± 0.005	349.67 ± 0.54	849.75 ± 0.75
	12.434 ± 0.007	324.98 ± 0.58	829.35 ± 0.44
	14.596 ± 0.014	300.56 ± 0.43	802.79 ± 3.18
Sn	25.007 ± 0.007	184.84 ± 0.29	689.09 ± 0.41
	28.329 ± 0.008	145.94 ± 0.48	650.75 ± 0.43

Table 4.2 Values of the means of the gaussian fits to the simulated and measured spectra.

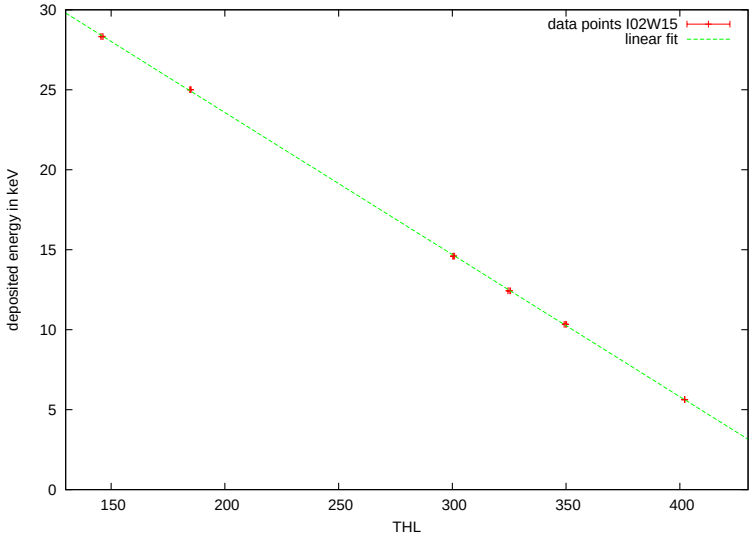

Figure 4.5 Calibration curve obtained by a THL-scan for detector I02W15.

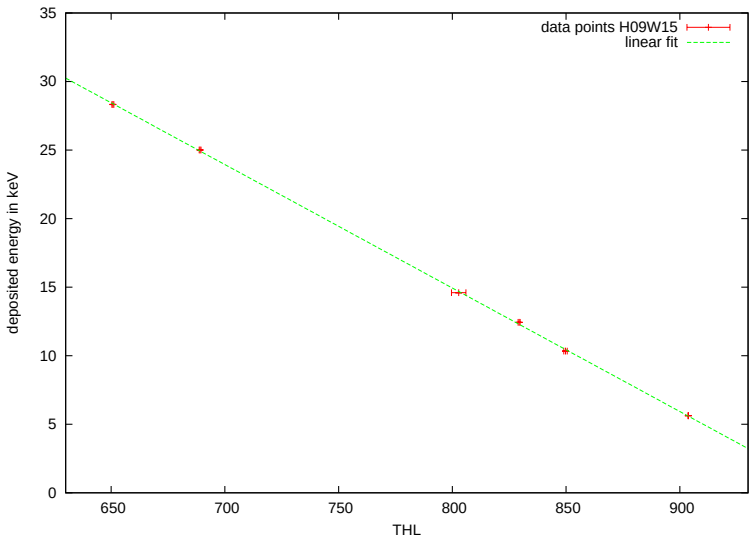

Figure 4.6 Calibration curve obtained by a THL-scan for detector H09W15.

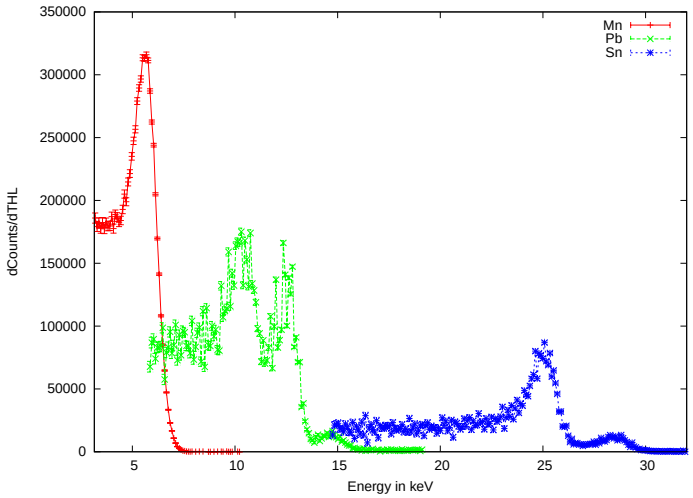

Figure 4.7 Measured THL spectra: Differentiated counts versus energy in keV (Detector I02W15).

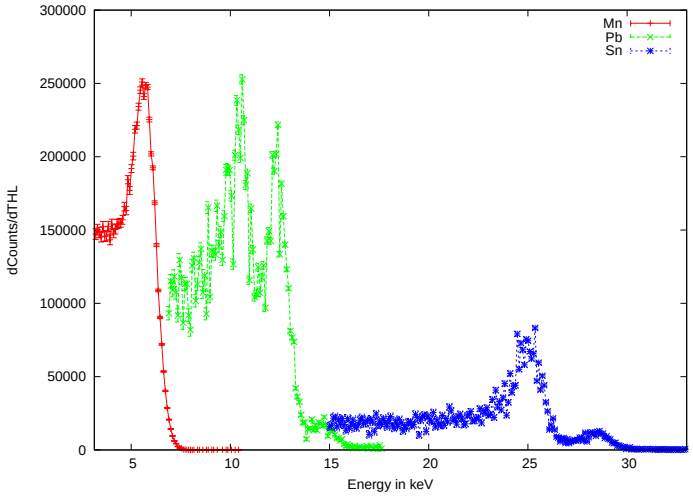

Figure 4.8 Measured THL spectra: Differentiated counts versus energy in keV (Detector H09W15).

4.3 Measurement of the detection efficiency

With these determined threshold energies the simulation is adapted to the different detectors. To check the correctness of the simulation the detection efficiency of both detectors is measured and compared to the simulation. For this purpose a mount for the given geometry of the source was designed, containing of a PVC-base fixed on the sensor board, four aluminum tubes and a PVC-holder, where the source is put in (see figure 4.9).

The distance from the sensor layer to the source was chosen be be about 10 cm, which has mainly three reasons:

1. As the number of photons impinging on the sensor layer scales approximately with $\frac{1}{d^2}$, where d is the distance from source to detector, the uncertainty of larger distance has less effect on the error of the solid angle acceptance.

2. The flux on the sensor layer is reduced and the whole pixel matrix is nearly equally illuminated. Although the flux on the sensor layer is reduced by the distance the required measurement is still within reasonable time.

3. The low energy electrons emitted by the source are not able to reach the detector.

The geometry of the source can be seen in figure 4.10. The radioactive substance is embedded between two polyethylene (PE) foils of $(23.40 \pm 0.07)\,\mu$m thickness each. The surrounding ring structure is made of aluminum. This is also taken into account in the simulation.

Simulation The whole setup described above was reproduced in the simulation, where the source was modeled as s ConicalSource (see [15]) with a radius of 2.5 mm and negligible thickness (FLT_EPSILON). It emits the particles isotropically. The two values needed from the simulation are the solid angle acceptance and the number of detected photons by a pixelated X-ray detector. For the first value an all interaction detector (AllIADetector) (see [15]) counts all the photons impinging on the sensor layer. Thus, the angular acceptance ϵ is given as the counts of the all interaction detector N_{AI} divided by the number of photons simulated $N_{\mathrm{simulated}}$:

$$\epsilon_{\mathrm{SA}} = \frac{N_{\mathrm{AI}}}{N_{\mathrm{simulated}}} \tag{4.3}$$

For the detection efficiency the response of the Timepix device was simulated and ASCII output files are created, containing the x and y values and the energy deposited in the pixel. Then the clustering algorithm described in [7], chapter IV, was used. In this simulated data no clusters with more than two entries were found. Thus, the number of

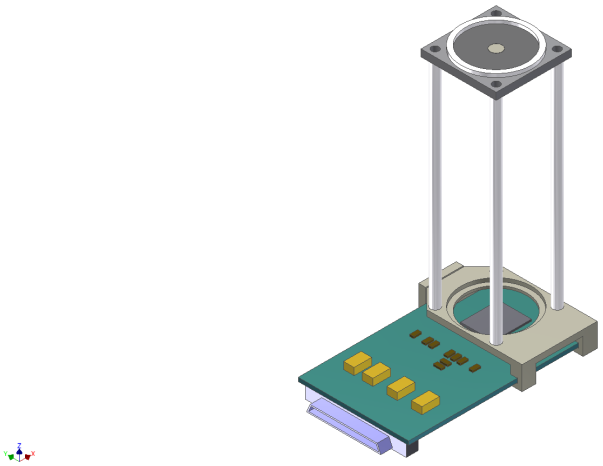

Figure 4.9 Stack for the measurement of the detection efficiency. A detailed drawing with all needed distances is shown in the appendix.

clusters N_{clusters} with less than three entries was counted. The detection efficiency can then be calculated by the formula

$$\epsilon_{\text{det}} = \frac{N_{\text{clusters}}}{N_{\text{AI}}} \tag{4.4}$$

with a statistical uncertainty of $\Delta\epsilon_{\text{det}} = \frac{\sqrt{N_{\text{clusters}}}}{N_{\text{clusters}}}$. The systematical error of the simulation is estimated by simulating the detection efficiencies for the lower and upper one sigma confidence levels of the threshold energy given in chapter 4.2.

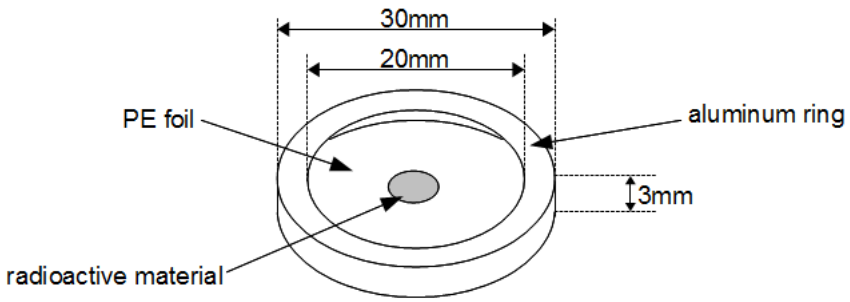

Figure 4.10 The geometry of the source carrier.

Detector	t_{frame} in s	U_{Bias} in V	f_{clock} in MHz
I02W15	1.000000	100	48
H09W15	1.000000	100	48

Table 4.3 Settings for the efficiency measurements for both detectors.

Measurements The measurements were performed in ToT mode with the settings shown in table 4.3.

To estimate the detection efficiency from the measurement the simulated solid angle acceptance ϵ_{SA}, the activity of the source A_{source}, the measured time t_{eff} and the fluorescence yield $\omega_{K_{\alpha,\beta}}$ are needed. Analogue to the simulation, the data is clustered and afterwards the cluster with less than three entries are counted, as the simulation results only contain these clusters with multiplicities one or two (The values can be taken from the statistics box in figure 4.12). One finds

$$\epsilon_{\text{det}}^{\text{meas}} = \frac{N_{\text{cluster}}^{\text{meas}}}{\omega_{K_{\alpha,\beta}} \cdot A_{\text{source}} \cdot t_{\text{eff}} \cdot \epsilon_{\text{SA}}}. \tag{4.5}$$

The statistical uncertainty is $\Delta\epsilon_{\text{det}}^{\text{stat}} = \epsilon_{\text{SA}} \cdot \frac{\sqrt{N_{\text{cluster}}^{\text{meas}}}}{N_{\text{cluster}}^{\text{meas}}}$. The calculation of the systematic uncertainty is explained below.

The activity of the ^{55}Fe-source is given by

$$A(t) = A_0 \cdot e^{-\frac{(t-t_0)\cdot \ln 2}{T_{1/2}}}, \tag{4.6}$$

where $A_0 = (72.5 \pm 1.1)$ is the activity at the time $t_0 = 1312156800$ in time to epoch, which corresponds to August 1$^{\text{st}}$, 2011 at 00:00 CET. The error on the activity is $\Delta A(t) = A(t) \cdot \frac{\Delta A_0}{A_0}$. As the time measured is short compared to the half life of this source the activity is assumed to be constant.

The error on the solid angle acceptance is estimated by simulating the source distances $d = 98.7\,\text{mm}$, $99.7\,\text{mm}$ (i.e. $100\,\text{mm}$ minus the thickness of the sensor layer) and $100.7\,\text{mm}$. Different reasonable radii of the source were found to have no impact on the result. Using the simulated result for the detection efficiencies at these distances, one finds asymmetric errors. Taking the distance $99.7\,\text{mm}$ as the relevant value gives: $\Delta\epsilon_{\text{SA},+} = \epsilon_{\text{SA},98.7\,\text{mm}} - \epsilon_{\text{SA},99.7\,\text{mm}}$ and $\Delta\epsilon_{\text{SA},-} = \epsilon_{\text{SA},100.7\,\text{mm}} - \epsilon_{\text{SA},99.7\,\text{mm}}$ (see table 4.5). The systematical errors of the detection efficiencies are calculated using the upper limits of the solid angle acceptance and the one sigma upper limit of the activity, and a second time with the corresponding lower ones.

	ϵ_{SA}	t_{eff} in s	A_{mean} in kBq	$N^{\mathrm{meas}}_{\mathrm{clusters}}$
I02W15	$0.001166^{+0.000016}_{-0.000023}$	216313.000000	61.67 ± 0.94	3993774 ± 1998
H09W15	$0.001166^{+0.000016}_{-0.000023}$	220000.000000	61.37 ± 0.93	4056454 ± 2014

Table 4.4 Summary of the measured results. The activity given is the mean one and considered to be constant as the measured time is small compared to the half life of the ^{55}Fe source.

	$\epsilon^{\mathrm{simulated}}_{\mathrm{det}}$	$\epsilon^{\mathrm{meas}}_{\mathrm{det}}$
I02W15	$0.893 \pm \underbrace{0.008}_{\text{stat.}} \underbrace{^{+0.010}_{-0.016}}_{\text{syst.}}$	$0.904 \pm 0.0005^{+0.032}_{-0.026}$
H09W15	$0.866 \pm 0.008^{+0.043}_{-0.060}$	$0.907 \pm 0.0005^{+0.032}_{-0.026}$

Table 4.5 Comparison of the simulation and measurement. See text for details on the error calculation.

The measured results are summarized in table 4.4 and compared to the simulated ones in table 4.5.

These simulated and measured values are in good agreement within the given errors. The slightly higher detection efficiency for the device that has a higher threshold level is probably due to the fact that the device H09W15 is a bit more noisy than I02W15, especially when using ToT mode with low threshold and high clock frequency.

Now to check the correctness of the cut on clusters with multiplicities one or two the simulated distribution of cluster sizes is compared to the measured one (see figure 4.11).

These distributions have slight differences. The simulated one shows more clusters with two hits, whereas the measured curve has a minimal higher probability for clusters with one hit. Another difference is that in the measurement, clusters with three or more entries can be found, that are due to the cosmic myon background, which can be seen by using the ToT information. Therefore the distribution of ToT counts per event, which is the sum of the counter values in the track, is plotted for clusters with less than three (figure 4.12) and three or more entries (figure 4.13).

The distribution of clusters with multiplicities one or two shows a clear peak in the lower energy region that is caused by the fluorescence X-rays from the manganese. On the other side in figure 4.13 one finds the typical Landau-distribution for the deposited energy of the myons and, what is more important, is the fact that there are just three counts (detector I02W15) and six counts (detector H09W15) in the lower energy region, that might be due to the manganese X-rays. So the loss of events caused by the cut on clusters with one or two entries can be estimated as $\frac{3}{3993772} = 8 \cdot 10^{-7} \approx 0$ (detector I02W15) and $\frac{4}{4056454} = 1 \cdot 10^{-6} \approx 0$, respectively.

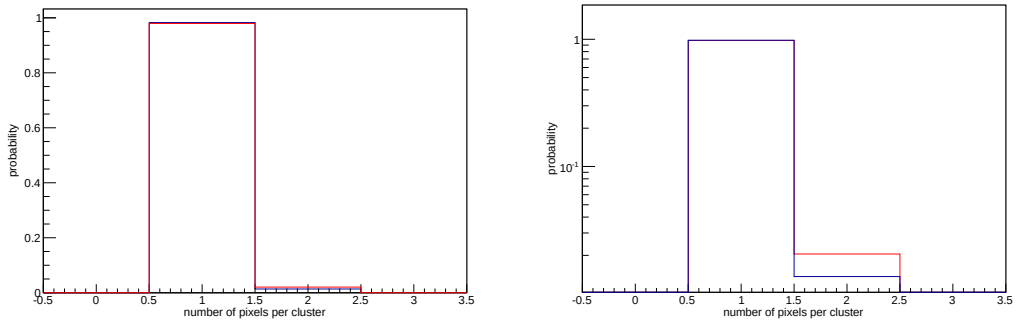

Figure 4.11 Comparison of the simulated (red) and measured (blue) distributions of cluster sizes. In the right plot a logarithmic scale for the y-axis is chosen to point out the difference of this distributions.

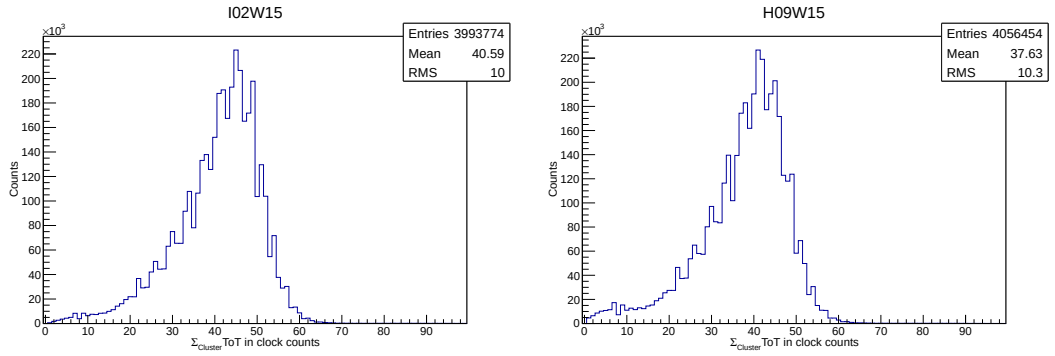

Figure 4.12 Spectrum of the clusters with multiplicities one or two of detector I02W15 (left) and H09W15 (right). The individual ToT values of each pixel in the cluster are summed up and the filled into the histogram. The entries values given in the statistics box are the numbers of singles used for calculation of the detection efficiencies.

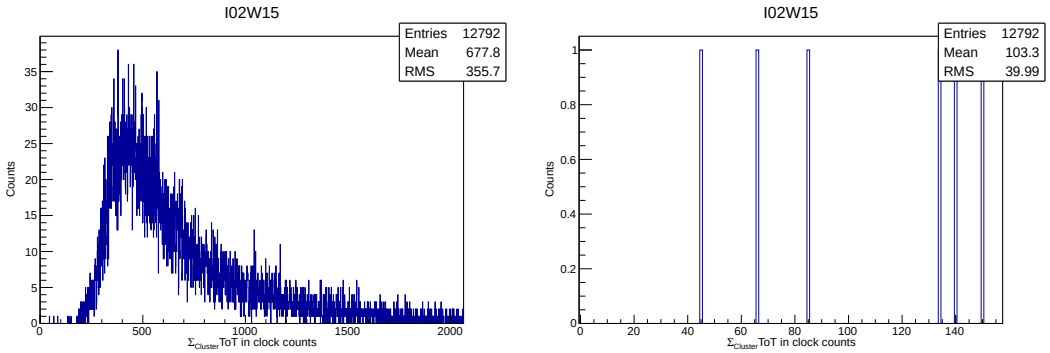

Figure 4.13 The spectrum of ToT values for clusters with sizes bigger than two. The ToT values of each pixel in one cluster are summed up and them filled into the histogram. The spectrum on the left shows the expected Landau-distribution of the energy deposited in the detector by myons. On the right a zoom into the region where the manganese X-rays should be found is done. Here just three entries are found that might be due these X-rays, that can be neglected compared with the 3993774 clusters with multiplicities one or two. These plots are done for detector I02W15.

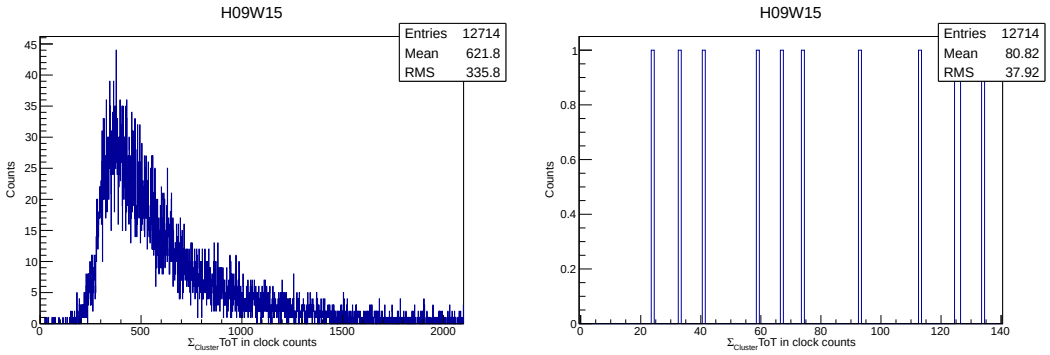

Figure 4.14 The spectrum of ToT values for clusters with sizes bigger than two. The ToT values of each pixel in one cluster are summed up and them filled into the histogram. The spectrum on the left shows the expected Landau-distribution of the energy deposited in the detector by myons. On the right a zoom into the region where the manganese X-rays should be found is done. Again, just six entries are found that might be due these X-rays, that can be neglected compared to the 4056454 clusters with multiplicities one or two. These plots are done for detector H09W15.

4.4 Estimation of the thicknesses of the Kapton foils

As the manufacturer's tolerances on the thicknesses of the Kapton-foils are too huge for our experiment, the thicknesses of the foils have to be estimated with smaller errors. Therefore, different more or less quadratic pieces (5.1 cm times 4.9 cm (HN50), 4.95 cm times 4.95 cm (HN100) and 5.00 cm times 5.05 cm(HN200)) were cut out of the foils used in the experiments and weighted. Knowing the density of the material $\rho_{\text{Kapton}} = 1.4200 \pm 0.0007 \frac{\text{g}}{\text{cm}^2}$ ([21], [22]) quite exact the thickness of the foil can easily be estimated by the formula $d_{\text{Kapton}} = \frac{m_{\text{Kapton}}}{\rho_{\text{Kapton}} \cdot A}$ with an error $\Delta d_{\text{Kapton}} = d_{\text{Kapton}} \cdot \sqrt{(\frac{\Delta\rho}{\rho})^2 + (\frac{\Delta m}{m})^2 + (\frac{\Delta A}{A})^2}$. The results are summarized in table 4.6 and compared to the thicknesses provided by the manufacturer "du Pont" [21].

	m in mg	A in cm^2	d_{Kapton} in μm	$d_{\text{Kapton}}^{\text{du Pont}}$ in μm
HN50	43.445 ± 0.001	24.99 ± 0.71	12.2 ± 0.3	$12.7^{+3.8}_{-3.7}$
HN100	85.367 ± 0.001	24.50 ± 0.70	24.5 ± 0.7	25.4 ± 3.8
HN200	181.951 ± 0.001	25.25 ± 0.71	50.7 ± 1.4	$50.6^{+6.4}_{-6.3}$
HN50+HN100	$d_{\text{HN50+HN100}} = (36.7 \pm 0.8)\,\mu$m			

Table 4.6 Results of the determination of the thickness of the Kapton foil. For the measurement with the single sided stack the Kapton-foils HN50 and HN100 were put on top of each other to get the thickness of $(36.7 \pm 0.8)\,\mu$m, where the error is calculated by the gaussian error propagation.

4.5 Results of the onesided-stack

4.5.1 Overview of the measurements

To show that the detector is capable to measure the hypersatellite-satellite coincidence, first a single sided stack was set up. Another PVC holder was designed for the given geometry of the source (see figure 4.15). The detector I02W15 was used and ToA-measurements without and with a Kapton foil of thickness 36.7 μm between source and sensor layer were performed. This thickness of the foil was reached by putting two foils, Kapton HN50 and Kapton HN100, on top of each other.

The relevant settings of the measurement are shown in table 4.7. Here burst-mode was used, so that readout frequencies up to 93 frames per second could be achieved.

An overview over the taken measurements with and without the Kapton-foil, the activity of the source, the numbers of single hits detected and the effective time measured are given in tables 4.8 and 4.9.

For the clustering the algorithm described in [7], chapter IV was used. The times are calculated with the maximum counter value $\mathrm{ToA}_{\mathrm{max}} = 11500$ that was taken into account in the evaluation , i.e. $t_{\mathrm{eff}} = N_{\mathrm{frames}} \cdot \frac{11500}{48\,\mathrm{MHz}}$.

4.5.2 Comparison between experiment and simulation

For simulating the detection yields δ_{i} again ROSI was used. The source was modeled as described in section 4.3. The PVC-holder, the chipboard and the source carrier with the aluminum ring as well as the two PE-foils were simulated. The detection yields are calculated as the number of detected particles divided by the number of simulated particles: $\delta_{\mathrm{i}} = \frac{N_{\mathrm{det,i}}}{N_{\mathrm{sim,i}}}$ (i $\in \{\gamma$, e-, IB$\}$).

The distance of the source and the shift of the detector in x- and y-direction were adjusted by comparing the simulation results with the measured data for the distribution of counts per row (pixel y) and column (pixel x). The distance of source and detector was found to be (4.63 ± 0.30) mm. To evaluate the effects of this uncertainty and the error on the thickness of the Kapton-foil the simulation was done three times for the distances

f_{clock} in MHz	U_{Bias} in V	t_{frame} in μs
48	100	240

Table 4.7 Setting used for the one-sided readout stack with the detector I02W15. The bias voltage is provided by the FitPix readout. The data was taken using the ToA-mode of the Timepix detectors.

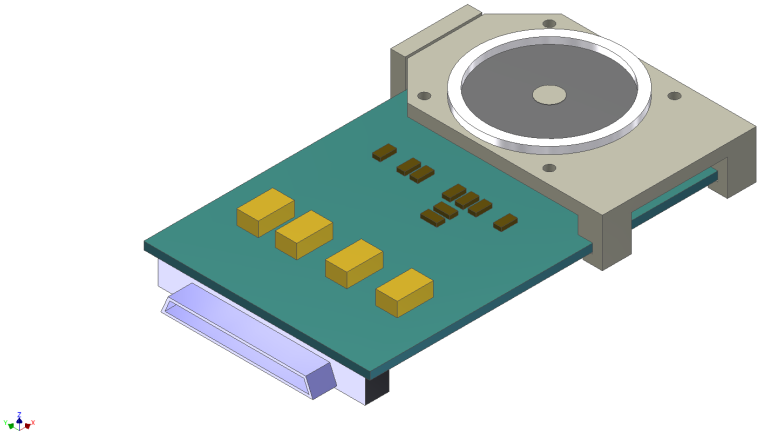

Figure 4.15 Stack used for the measurement with the one sided readout. A detailed drawing can be found in the appendix.

4.33 mm, 4.63 mm and 4.93 mm (the thickness of the foil was kept at 36.8 μm) and three times for thicknesses 36.0 μm, 36.8 μm and 37.6 μm (the distance was kept at 4.63 mm). The pixel x and pixel y distributions for the different settings of the simulation compared with the experimental data are shown in figure 4.16. As the variation of the Kapton thickness has no real effect on the detection yield for photons, this is not considered in this plot. For the electrons this is the main contribution to the uncertainty of detection yield.

The lower error limit is calculated as $\delta_{4.33\,\mathrm{mm}} - \delta_{4.63\,\mathrm{mm}}$, the upper error limit as $\delta_{4.93\,\mathrm{mm}} - \delta_{4.63\,\mathrm{mm}}$ which is equal to each other in the chosen accuracy. This is done in the

Date	Activity of the source in kBq	Measured time s
02/12/2011	66.47 ± 1.01	3452.4
05/12/2011	66.33 ± 1.01	3452.4
$\langle A_{\mathrm{source}} \rangle \pm \langle \Delta A_{\mathrm{source}} \rangle = (66.40 \pm 1.01)\,\mathrm{kBq}$		
$N_{\mathrm{DL}} = 25771387 \pm 5077$		
$t_{\mathrm{eff}} = 6904.8\,\mathrm{s}$		

Table 4.8 Measurements without the Kapton-foil. The dates of the measurement, the actual activity of the radioactive source and the effective measuring time are given for each run individually as well as for the whole measurement. Also the number of detected clusters with multiplicities one or two is shown.

Date	Activity of the source in kBq	Measured time s
16/12/2011	65.82 ± 1.00	1878.3
19/12/2011	65.68 ± 1.00	3452.4
23/12/2011	65.49 ± 0.99	3378.1
26/12/2011	65.36 ± 0.99	3452.4
29/12/2011	65.22 ± 0.99	3452.4
01/01/2012	65.08 ± 0.99	3452.4
04/01/2012	64.94 ± 0.99	3452.4
09/01/2012	64.72 ± 0.99	3452.4
12/01/2012	64.58 ± 0.99	3452.4
$\langle A_{\text{source}} \rangle \pm \langle \Delta A_{\text{source}} \rangle = (65.21 \pm 0.99)\,\text{kBq}$		
$N_{\text{DL}}^{\text{Kapton}} = 95612245 \pm 9778$		
$t_{\text{eff}} = 29423.23\,\text{s}$		

Table 4.9 Measurements with Kapton-foil of thickness 36.7 μm. The dates of the measurement, the actual activity of the radioactive source and the effective measuring time are given for each run individually as well as for the whole measurement. Also the number of detected clusters with multiplicities one or two is shown.

	δ_γ	$\delta_\gamma^{\text{Kapton}}$
simulated	0.201 ± 0.010	0.179 ± 0.009
measured	0.198 ± 0.006	0.175 ± 0.005

Table 4.10 Comparison of simulated and measured acceptances.

same way for the different thicknesses of the Kapton-foil. The errors due to the thickness of the foil and due to the distance are summed up.

To check the simulation results, the simulated and measured detection yields for the fluorescence photons are compared. The measured ones are calculated by the formula for the rate of the diagram line photons: $\delta_\gamma = \frac{N_{\text{DL}}^{\text{meas}}}{t_{\text{eff}} \cdot \omega_{\text{K}_{\alpha,\beta}} \cdot A_{\text{source}}}$. The error is given by $\Delta\delta_\gamma = \delta_\gamma \cdot \sqrt{(\frac{\Delta N_{\text{DL}}^{\text{meas}}}{N_{\text{DL}}^{\text{meas}}})^2 + (\frac{\Delta A_{\text{source}}}{A_{\text{source}}})^2}$ (see table 4.5.2). The simulated and measured values were found to be in a good agreement.

4.5.3 Spectrum of the time-differences

As the distribution of the detection times shows a peak at the end of the ToA spectrum (see figure 4.17), that is due to events detected before the frame was opened, the maximum counter value taken into account for further evaluation was set to 11500 to ignore these events.

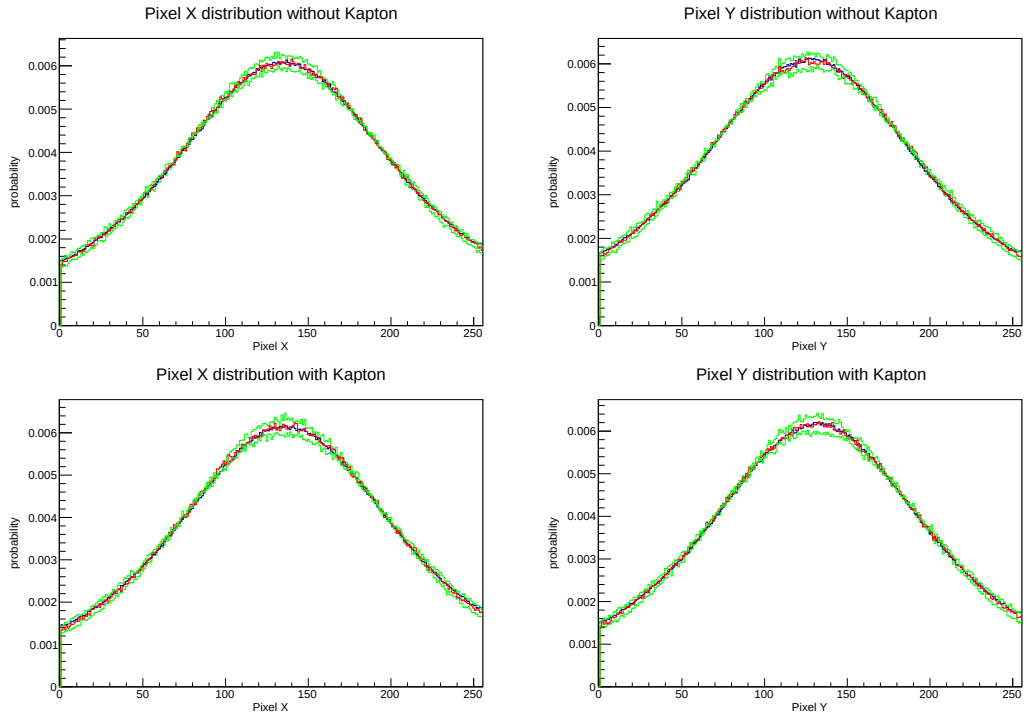

Figure 4.16 Comparison of the simulated (green, red) and measured (blue) pixel X and pixel Y distributions. The green curves show the upper and lower limits obtained by varying the distance to the detector.

The frames are divided into ten subframes, each with a maximum counter value of 1150, to minimize the loss due to an additional random fluorescence photon in the frame. This is illustrated in figure 4.18 and only subframes with exactly two clusters with multiplicities one or two are selected.

The choice for this number of divisions has mainly three reasons:

1. The loss of the signal decreases with increasing number of divisions: For lower values than ten the loss of the signal is quite high ($\gg 10\%$), whereas higher values do not decrease this loss significantly.

2. The signal to noise ratio decreases with increasing number of divisions. As more division mean steeper slopes of the background fit (see below figures 4.20 and 4.21), the errorbars in the region of interest of the extrapolated curves increase, and, in the same way, the errors on the measured numbers of events in the coincident peaks.

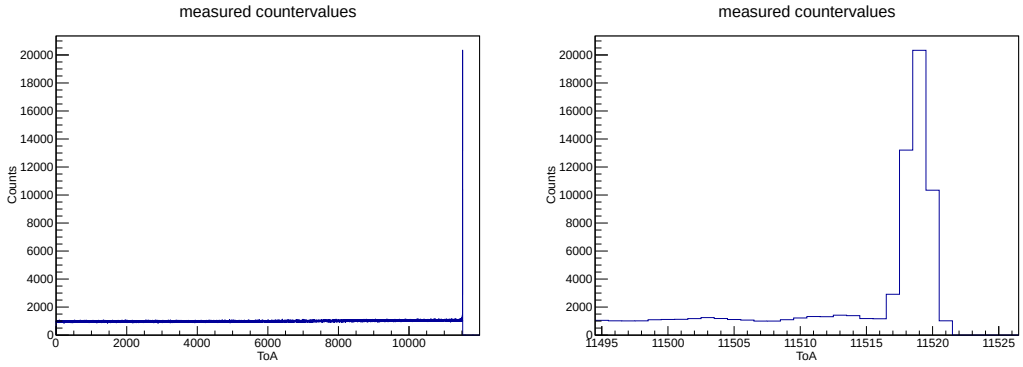

Figure 4.17 Spectrum of the measured ToAs for the one sided readout. The left figure shows the whole spectrum. On the right side a zoom into the region of higher ToAs is done to show the peak due to particles impinging on the detector before the frame was opened. All events with counter values above 11500 are neglected.

3. In the evaluation of the final double sided stack (see chapter 5) the maximum ToA used for the evaluation was set to 11090. As this value can be divided by ten getting an integer number, one avoids the problem of losing acquisition time by this division, which may cause problems when comparing the numbers of coincident events with the number of K diagram line photons.

In these subframes the time-differences $\Delta\text{ToA} = \text{ToA}_1 - \text{ToA}_2$ between two hits are calculated and filled into a histogram. In the case that the cluster with multiplicities one or two contains two entries, the higher ToA of this cluster, meaning the earlier event, is used to calculate this difference. In this way the influence of the time-walk effect is minimized. The coincidences are seen in the peak around 0. This procedure is done for the measurement with and without the Kapton-foil (see figure 4.19).

The triangular shape of this spectrum can be explained by a convolution of two uniformly distributed random ToA-variables. The shape is described by the function $f(\Delta\text{ToA}) = y_0 - m \cdot |\Delta\text{ToA}|$, where m is the slope, and y_0 is the y-axis-intercept. This function is then fitted to the background of random events ($\Delta\text{ToA} < -5$ and $\Delta\text{ToA} > 4$), and extrapolated into the region of interest, i.e. $\Delta\text{ToA} \in [-5; 4]$ (see figures 4.21 and 4.20).

The number of events in the coincidence peak is calculated as the differences of the bin contents of the measured spectrum $h^{\text{i}}_{\text{meas}}$ and the fitted ones $h^{\text{i}}_{\text{fit}}$:

$$N^{\text{peak}}_{\text{meas}} = \Sigma^{4}_{i=-5} h^{\text{i}}_{\text{meas,}} - \Sigma^{4}_{i=-5} h^{\text{i}}_{\text{fit}} = N_{\text{meas}} - N_{\text{fit}}. \tag{4.7}$$

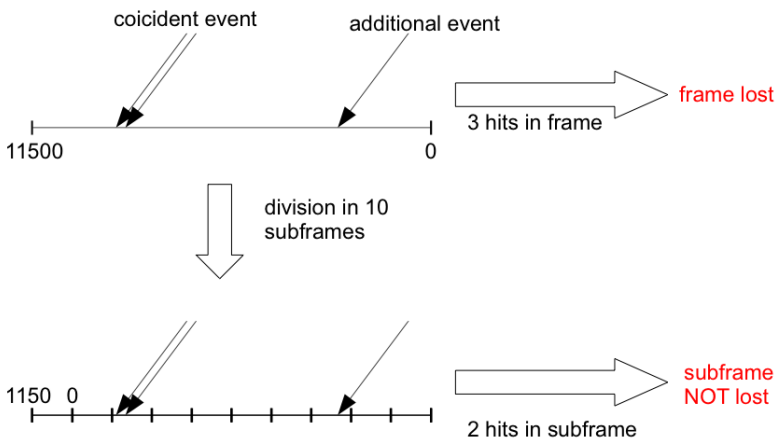

Figure 4.18 The frames are divided into ten subframes to decrease the loss due to an additional event from another atom in the same frame.

	with foil	without foil
$N_{\text{meas}}^{\text{peak}}$	515 ± 175	240 ± 97
t_{eff} in s	29234.23	6904.80

Table 4.11 Number of events in the coincidence peak.

The error of $N_{\text{meas}}^{\text{peak}}$ is given by $\Delta N_{\text{meas}}^{\text{peak}} = \sqrt{N_{\text{meas}} + \left(\Sigma_{i=-5}^{4} \Delta h_{\text{fit}}^{\text{i}}\right)^2}$ where $\Delta h_{\text{fit}}^{\text{i}}$ are the one sigma confidence levels also shown in figures 4.20 and 4.21. The measured numbers are given in table 4.11. [1]

These numbers need to be corrected due to the loss because of accidental additional fluorescence photons in the frame and loss at the edges of the subframes. Therefore a simulation was written that is described in the next chapter.

[1] As the focus of this work is on the high precision measurement (see chapter 5) with the double sided stack, for the final evaluation of the data from the one sided stack the same limits for the background fit and the range of the signal were used.

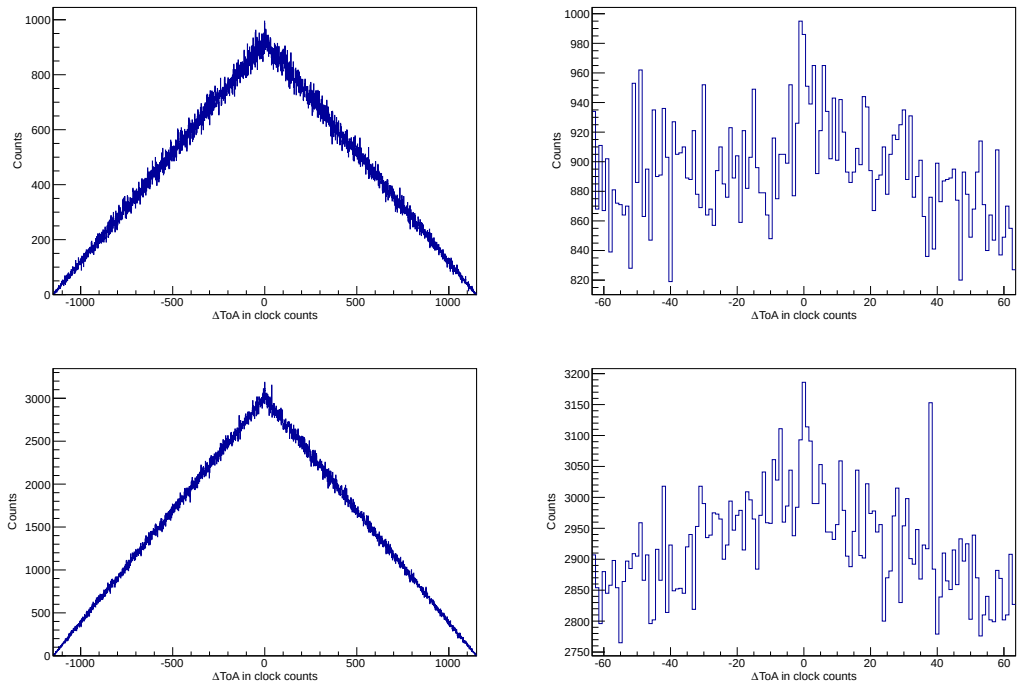

Figure 4.19 Spectrum of the time differences for the measurement without (upper histograms) and with (lower ones) the Kapton-foil. On the left the whole spectrum with triangular shape is shown and on the right a zoom into the region of interest.

4.5.4 Simulation to estimate the loss of the signal

As it can happen, that a coincident event is in a subframe that contains three or more entries, this loss has to be estimated. This is done by a simulation:

First, the number of hits per frame N_{HPF} is calculated from the measured number of clusters with multiplicities one or two per frame and the known number of frames that were measured. The user can set the number of photons that shall be simulated N_{simu}. With that information the number of simulated frames is given by $N_{\mathrm{simu}}^{\mathrm{frames}} = \frac{N_{\mathrm{simu}}}{N_{\mathrm{HPF}}}$. Afterwards N_{simu} times a uniformly distributed random integer variable X between zero and $X_{\mathrm{max}} = N_{\mathrm{simu}}^{\mathrm{frames}} \cdot \mathrm{ToA}_{\mathrm{max}}$ is generated using the TRandom3 class of ROOT [19] and divided by the maximum ToA of a frame ($\mathrm{ToA}_{\mathrm{max}}$) to assign it to a frame number. The ToA in this frame is calculated as $\mathrm{ToA} = X \mod \mathrm{ToA}_{\mathrm{max}}$. This data is then stored in an array of vectors where the index of the vector denotes the frame number. The size of each vector gives the number of hits per frame, and the entries of the vectors contain the

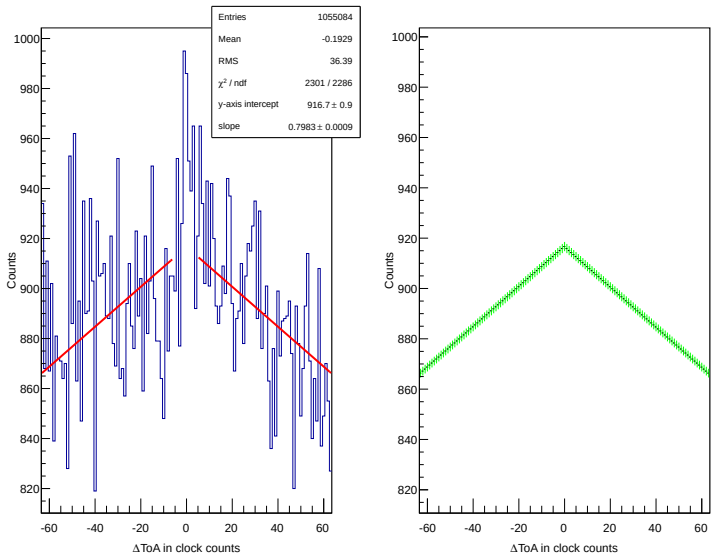

Figure 4.20 Fit to the background of random events (left) and extrapolation with the one sigma confidence levels into the region of interest (right) for the measurement without the foil.

ToA-information.

To model the signal in about $P_{\text{Signal}} \approx 10^{-5}$ times not only one photon is generated, but also a second one with a ToA that is randomly gaussian distributed around the first ToA, with a standard deviation 1.2 for the measurement without the foil, where electrons contribute to the signal and thus broaden the peak, and 0.8 for the measurement with the Kapton foil, respectively (see also [10], chapter 7). The P_{Signal}-values were tuned in order to describe the measured quantities.

If the frame numbers of these two coincident events are different, the event is lost and the counter for the loss of signal is incremented by one. The frame numbers of the signal events and the ToA-values are stored in a second array of vectors. If the given number photons N_{simu} is simulated, the same evaluation as described above - with the division into subframes and then cutting on the subframes, that contain exactly two hits - is performed. To estimate the loss of the signal, one has to look at the subframes that are given by the stored values of the coincident events, the frame number and the ToA-values. If the relevant subframes contain more than two hits again the counter for the loss of

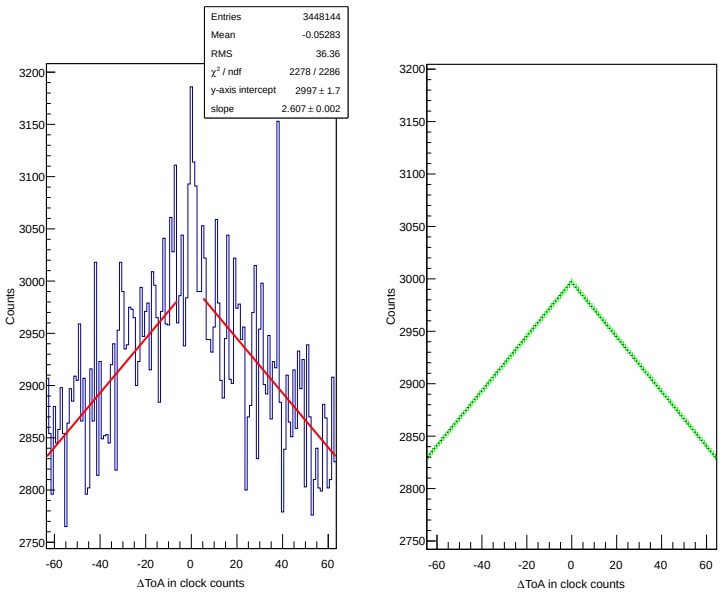

Figure 4.21 Fit to the background of random events (left) and extrapolation with the one sigma confidence levels into the region of interest (right) for the measurement with the foil.

signal is incremented by one.

Finally, the probability of the edges losses and losses due to additional events in the frame is calculated as the fraction of the number of lost ones and the simulated number of coincident events $P_{\text{loss}} = \frac{N^{\text{loss}}_{\text{counter}}}{N^{\text{simulated}}_{\text{coinc}}}$. To compare the simulation with the measured results the simulation also provides the spectrum of time differences and the information about the distribution of the number of clusters with multiplicities one or two in one frame. This is shown in figures 4.22 and 4.23, where the red curves are simulation and the blue ones are measured results.

To estimate the uncertainties of this estimation, the simulation is done several times and the standard deviation of the obtained values is taken as the error. As the relation of number of single hits to number coincidences as well as the width of the peak is different for the measurements with and without the foil this has to be simulated separately. The values obtained are given in table 4.12.

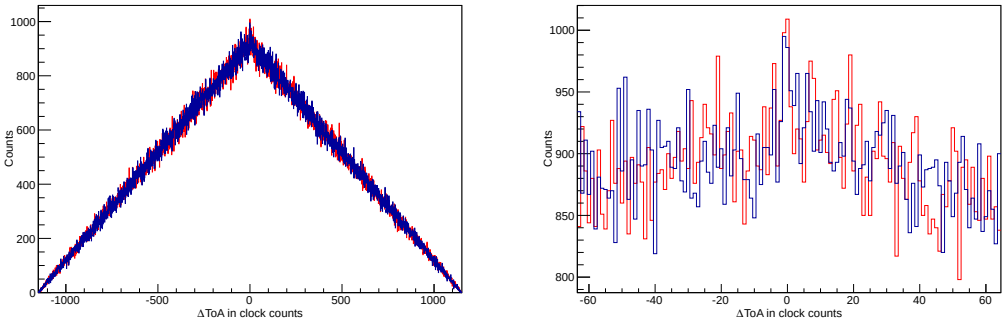

Figure 4.22 Comparison of the simulated (red) and measured (blue) spectra of the ToA differences. The full spectra can be seen in the left plot, a zoom into the region of interest is shown on the right.

	with foil	without foil
P_{loss}	0.073 ± 0.002	0.082 ± 0.003

Table 4.12 Simulated results for the loss of signal due to additional event in the same frame.

4.5.5 First result on P_{KK}

With the knowledge of how the measured numbers have to be corrected the formula for P_{KK} can be written as

$$P_{\text{KK}} = \frac{\frac{N_{\text{peak}}^{\text{meas,Kapton}}}{N_{\text{DL}}^{\text{Kapton}} \cdot (1 - P_{\text{loss}}^{\text{Kapton}})} - \frac{\delta_{\text{e-}}^{\text{Kapton}} N_{\text{peak}}^{\text{meas}}}{\delta_{\text{e-}} \cdot N_{\text{DL}} \cdot (1 - P_{\text{loss}})} - \delta_{\text{IB}} P_{\text{IB}} (1 - \frac{\delta_{\text{e-}}^{\text{Kapton}}}{\delta_{\text{e-}}})}{\alpha_\gamma - \alpha_\gamma^{\text{Kapton}} \cdot \frac{\delta_{\text{e-}}^{\text{Kapton}}}{\delta_{\text{e-}}}}. \tag{4.8}$$

The missing detection yields for the electrons and the Internal Bremsstrahlung-photons are simulated using the spectra given in section 3. The measured and simulated results are summarized in table 4.13.

The statistical errors on P_{KK} are given by the uncertainties of the values $N_{\text{peak}}^{\text{meas}}$, N_{DL} and P_{loss}, with gaussian distributed errors. The systematical errors from the different acceptances are assumed to be uniformly distributed. To estimate the influence of these uncertainties on the error of the P_{KK}-value a C++-program is written, that generates random numbers, using again the TRandom3 class from the ROOT library, according to the assumed distributions and for various different combinations P_{KK} is calculated and filled into a histogram. This is done separately for the statistical and the systematical errors. The obtained distributions for P_{KK} are normalized by the condition $\Sigma_i h_i = 1$ and shown in figure 4.24. h_i denotes the bin content of bin i.

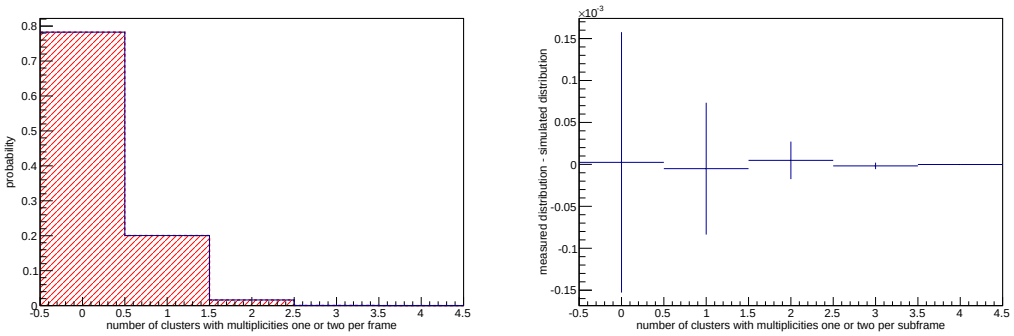

Figure 4.23 Simulated (red) and measured (blue) distributions for the number of clusters with multiplicities one or two in one subframe (left plot) and the difference of these distributions (right plot).

	with foil	without foil
$N_{\text{peak}}^{\text{meas}}$	515 ± 175	240 ± 97
N_{DL}	95612245 ± 9778	25771387 ± 5076
P_{loss}	0.073 ± 0.002	0.0848 ± 0.0008
δ_γ	0.179 ± 0.009	0.202 ± 0.010
$\delta_\gamma^{\text{HS}}$	0.187 ± 0.009	0.208 ± 0.011
$\delta_{\text{e-}}$	0.00020 ± 0.00001	0.00163 ± 0.00008
δ_{IB}	0.0125 ± 0.0008	0.0125 ± 0.0008

Table 4.13 Summary of the simulated and measured results.

The statistical errors have a symmetrical gaussian shape, wherefore the P_{KK} value is given by the mean and and the error by the standard deviation (see statistic box in figure 4.24). As the distribution of the systematical errors is asymmetric, the one sigma confidence levels around $P_{\text{KK}}^{\text{mean}}$ are determined from the equations

$$\Sigma_{\text{i}=P_{\text{KK}}^{\text{mean}}-\sigma_-}^{P_{\text{KK}}^{\text{mean}}} h_{\text{i}} = \frac{0.683}{2} \text{ and } \Sigma_{\text{i}=P_{\text{KK}}^{\text{mean}}}^{P_{\text{KK}}^{\text{mean}}+\sigma_+} h_{\text{i}} = \frac{0.683}{2}. \tag{4.9}$$

Finally one obtains as a first result

$$P_{\text{KK}} = (0.788 \pm \underbrace{0.383}_{\text{stat.}} \underbrace{^{+0.029}_{-0.027}}_{\text{syst.}}) \cdot 10^{-4}. \tag{4.10}$$

The value obtained is lower than the values of other experiments (see chapter 2.1), but, as the errors of the measurements are quite huge, they overlap in a one sigma confidence level. The most important fact concerning this result is that the systematical error is not

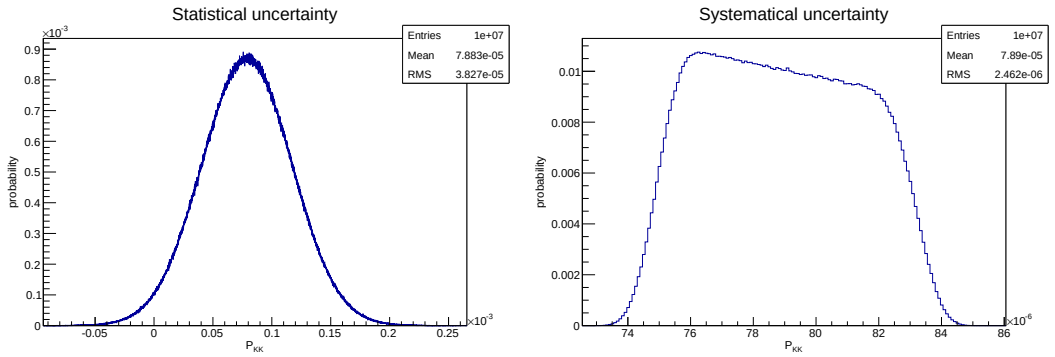

Figure 4.24 Distribution of the P_{KK}-values taking into account the statistical errors (left) and the systematical ones (right).

just an order below the statistical one, but also one order below the errors given in the literature. That means with more statistic (more measuring time and/or higher solid angle acceptance) one may be able to decrease the current error limits by a factor of five and get into the region where one is sensitive to the calculation method used (see figure 2.4 and chapter 2.1).

5 High precision measurement of the double K-shell vacancy production probability of ^{55}Fe

Contents

5.1 Trigger-circuit and automation of the measurements

For the next measurements a double sided stack was used (see figure 5.1), consisting of the two Timepix detectors described above, which are operated in coincidence. Therefore, a trigger circuit is needed. The trigger electronics scheme is shown in figure 5.2.

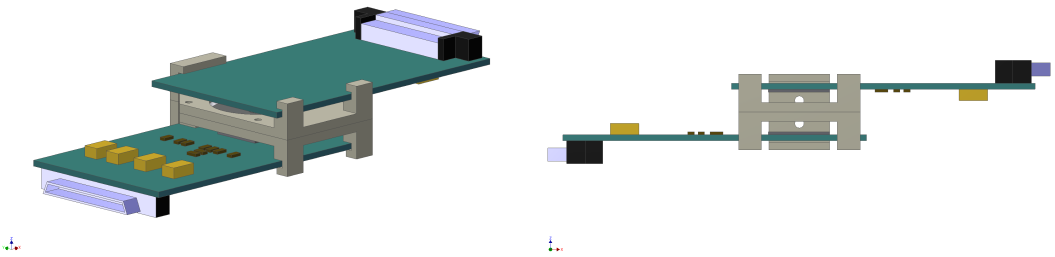

Figure 5.1 Drawing of the double sided stack seen from two different perspectives. The holders for the ^{55}Fe source were the same as in the one sided stack.

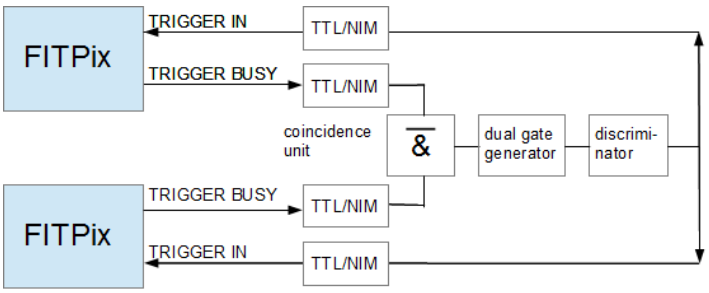

Figure 5.2 Scheme of the trigger electronics used to make the detectors work in coincidence.

	f_{clock} in MHz	U_{Bias} in V	t_{frame} in μs	THL
I02W15	48	100	204	430
H09W15	48	100	204	925

Table 5.1 Settings used for the measurement of cosmic myons with the double sided stack. 2210000 frames were taken.

For the triggering a simple anti coincidence is done for the TRIGGER BUSY signals from the two readouts (see also [13]). If both signals are in logic low, the coincidence unit gives a short logical pulse that is extended up to the frametime with a dual gate generator and a discriminator. Then it is sent to the readout inputs TRIGGER IN. Thus, the frametime is adjusted in the trigger circuit. Each time both readouts are capable of measuring, the frame is opened. For exchanging between the different logics (NIM and TTL-compatible CMOS) of the trigger circuit and the readout a NIM/TTL converter is used. [1]

To see if the trigger circuit works, a measurement in the double sided stack without the source was performed, measuring the tracks that are typical for myons. As cosmic myons travel nearly at the speed of light, they should be detected in both detectors at the same time. The details on this measurement can be found in table 5.1.

Only those myon events are taken into account, that have hit both detectors, with the consistent geometry. For the geometrical selection the distance between the two detectors is calculated using the information about the length of the tracks in the two detectors. Figure 5.3 illustrates the calculation:

First, the length of the tracks in the single detectors is calculated using $l^i_{\text{track}} = \sqrt{(x^{\max}_{\text{track}} - x^{\min}_{\text{track}})^2 + (y^{\max}_{\text{track}} - y^{\min}_{\text{track}})^2}$. If these distances are nearly the same in both detectors, the event is taken for further investigations and the mean value of both

[1] In the pixelman software the setting "started by HW-trigger, stopped by HW trigger" is used.

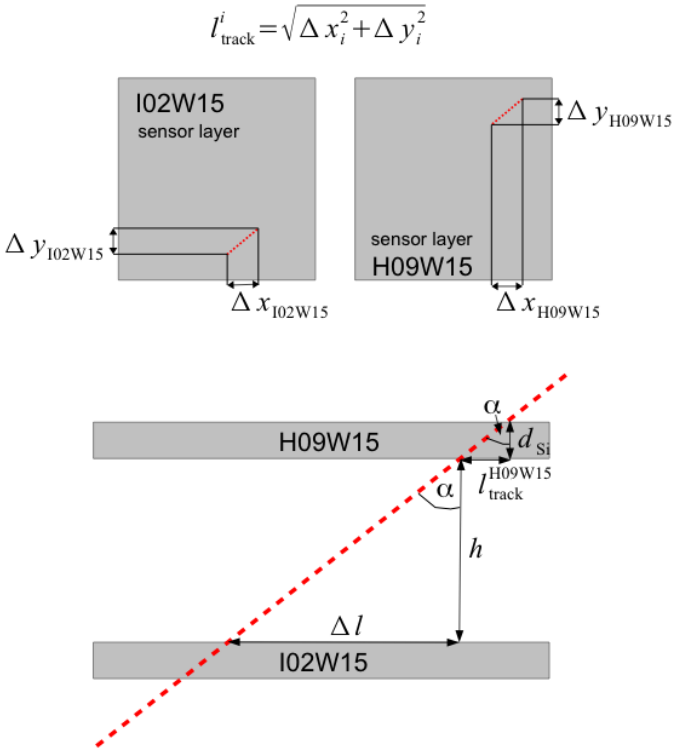

Figure 5.3 Illustration of the geometry of the stack and definitions of the values taken for the geometrical selection. The red dashed line indicates the myon track.

tracks l_{track} is calculated. Now $\Delta l = \sqrt{(x^{\text{H09W15}}_{\text{min}} - x^{\text{I02W15}}_{\text{max}})^2 + (x^{\text{H09W15}}_{\text{min}} - x^{\text{I02W15}}_{\text{max}})^2}$ is estimated. To test whether the hits in the detectors are from the same event, the distance between the detectors is determined from the geometry of the tracks, i.e.

$$\tan\alpha = \frac{\Delta l}{h} = \frac{l_{\text{track}}}{d_{\text{Si}}} \rightarrow h = \frac{d_{\text{Si}}}{l_{\text{track}}} \cdot \Delta l, \tag{5.1}$$

with $d_{\text{Si}} = 0.3\,\text{mm}$.

As the distance between the two detectors is approximately 1 cm, only those events are taken where the estimated distances are in the range $h \in [0.8\,\text{cm}; 1.2\,\text{cm}]$. By this method three events were found, which are shown in figure 5.4. Table 5.2 summarizes the geometrical situation for these three events labeled with their frame number. As the energy deposited in the sensor is Landau distributed and therefore has a wide range, for the myons the time walk effect is very dominant. Thus, the interesting ToAs are the

Frame number	l_{track} in pixel	Δl in pixel	h in cm
581388	3.50	119.50	1.02
1431798	2.24	61.40	0.82
2100876	3.35	104.00	0.93

Table 5.2 Values used to estimate the distance between the two detectors from observed myon tracks.

maximum ToAs of each track. As these arrival times in both detectors are the same or just differ by one clock count, which may be due to the trigger response, that can be up to 20 ns [13], the trigger circuit works properly.

As it is not very comfortable having to start the measurements manually for the long term measurement (the one with the Kapton foil) an AutoIt-script (see [23]) was written, that undertakes this task. [2]

[2] AutoIt is a quite simple software package that can be used in windows to simulate mouse clicks or key inputs (The whole script can be found in the appendix). It terminates the measurement with pixelman when the ASCII-file with the adjusted number of repeons is written to the disk, then enters the name for the following measurement, starts it and compresses the taken data into zip-files.

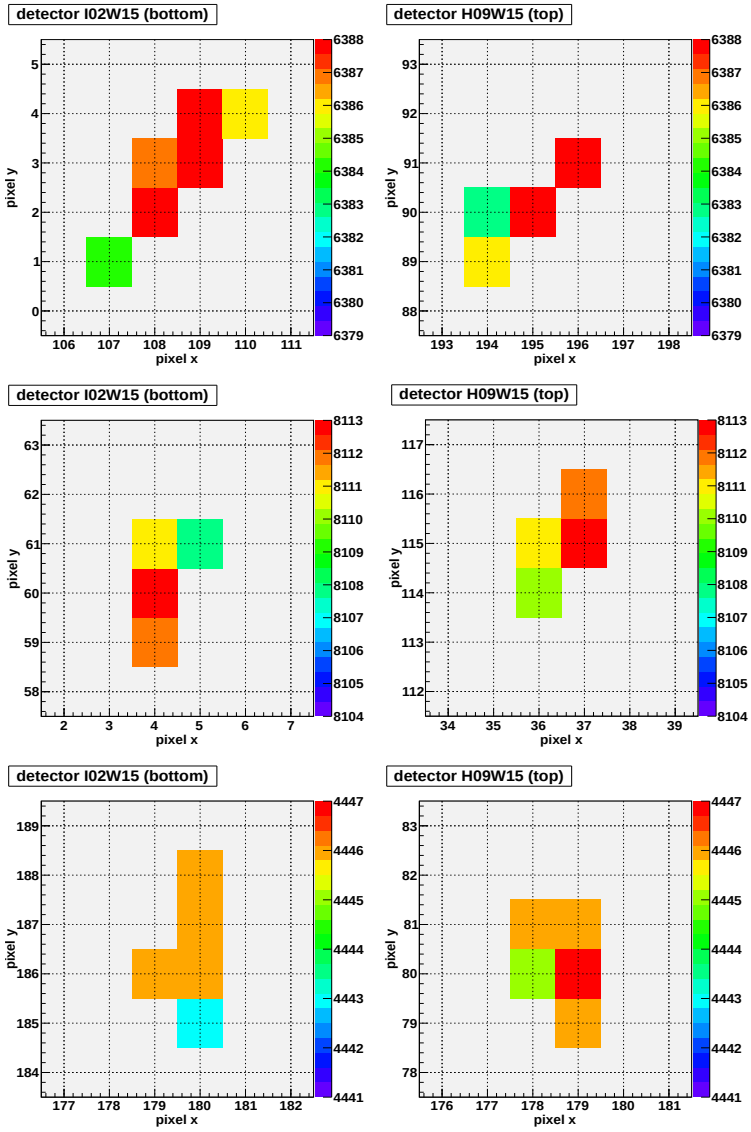

Figure 5.4 Coincident myon events, with the right geometry (see also table 5.2), that were used to check the performance of the trigger circuit. To see if the trigger works, the maximum counter values of these tracks in the different detectors have to be compared. The frame numbers of these events are 581388, 1431798 and 2100876 from top to bottom.

5.2 Reliability of the data taken from the double sided stack

Before the evaluation of the data of the final stack with the Kapton foil of thickness $(50.7 \pm 1.4)\,\mu$m, the stability of the detectors, as well as the reliability of the data was tested by plotting the number of clusters with multiplicities one or two in one run, containing 661 times 10000 frames, versus the time since the beginning of the measurement (see figure 5.5). An exponential fit $f(x) = A \cdot e^{-\frac{\ln 2}{T_{1/2}} \cdot t}$ to this data is done. By this one obtains as a half-life time $T_{1/2} = (2.75 \pm 0.07)$ a, which agrees well with the theoretical value.

The detectors are also evaluated separately (see figure 5.6). Here, the values found for the half lifes are $T_{1/2}^{\mathrm{I02W15}} = (2.9 \pm 0.1)$ a and $T_{1/2}^{\mathrm{H09W15}} = (2.5 \pm 0.2)$ a. Detector H09W15 shows larger deviations from the fit than I02W15 and the variations of the two detectors are not correlated. This leads to the conclusion, that they are probably due to fluctuations in the threshold level (see also 4.2), that are expected to be bigger for detector H09W15.

But, as the result of the fit for the whole statistic gives the predicted value, there is no systematical influence that has to be considered in the evaluation.

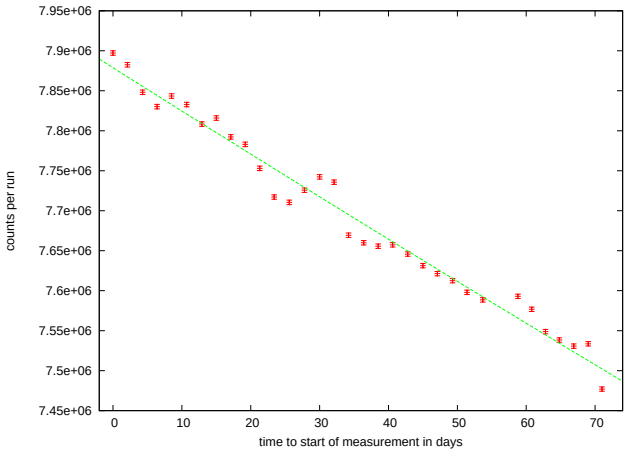

Figure 5.5 Plot of the clusters with multiplicities one or two per run versus the time to the start of measurement. The half life time of ^{55}Fe $T_{1/2} = (2.75 \pm 0.08)$ a is obtained by fitting an exponential law, which in in good agreement with the theoretical one.

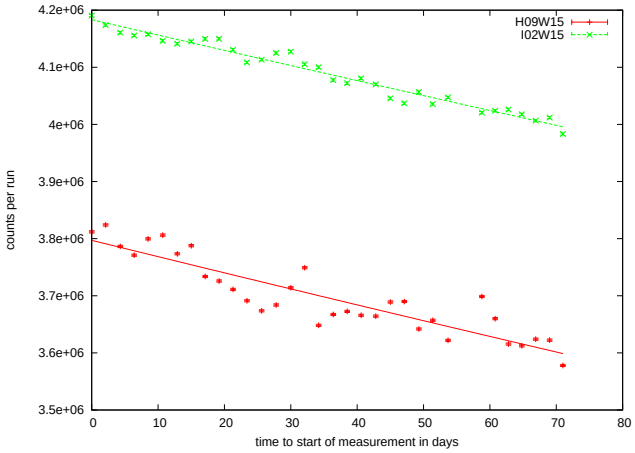

Figure 5.6 Clusters with multiplicities one or two per run versus time to the start of the measurement for each detector individually. The half lifes obtained by the fits are $T_{1/2}^{\mathrm{I02W15}} = (2.9 \pm 0.1)$ a and $T_{1/2}^{\mathrm{H09W15}} = (2.5 \pm 0.2)$ a.

5.3 Evaluation of the data from the double sided stack

The evaluation of the data from the double sided stack is done completely analogue to the one for the single sided stack described in chapter 4. First, to see if the detectors work properly and to get the alignment right, both detectors are considered separately. Afterwards the whole data is used to obtain a value with small errors.

5.3.1 Overview over the performed measurements

As with the one sided stack, again measurements with and without a Kapton foil were performed. But, as this data also shall be used to see an angular correlation between the fluorescence photons (see chapter 6), a thicker foil, $d_{\text{Kapton}} = (50.7 \pm 1.4)\,\mu$m (see section 4.4), was chosen in order to suppress the electronic background. For the long term measurement with the foil the data is divided into runs. Each run contains 661 repetitions with 10000 frames. The setting for the measurement with and without the foil are shown in table 5.3, where the frametime is adjusted by the trigger circuit (see 5.1).

As the acquisition time of the frames is shorter than in section 4, the maximum ToA taken into account in this case is set to 11090 for the measurement with the foil and 9770 for the one without the foil, respectively. This corresponds to maximum frametimes of $t_{\text{frame}}^{\text{Kapton}} = 231\,\mu$s and $t_{\text{frame}} = 203.5\,\mu$s. The counting of the runs of the Kapton-measurement starts at 7, because in runs 1 to 6 the detectors were not aligned properly, so that this data was not used. Tables B.1 and B.3 show the whole set of performed measurements. The data is shown for each detector individually as well a for the whole stack. For stability control purposes, the detection yields are calculated for each run individually. Their final values are calculated as the error-weighted means of the detection yields for each run (see tables B.2 and B.4). The following table 5.4 summarizes the main results.

	f_{clock} in MHz	U_{Bias} in V	t_{frame} in μs
without the foil			
I02W15	48	100	204
H09W15	48	100	204
with the foil			
I02W15	48	100	232
H09W15	48	100	232

Table 5.3 Settings used for the measurements of the double sided stack with and without the Kapton-foil of thickness $d_{\text{Kapton}} = (50.7 \pm 1.4)\,\mu$m.

	without foil	with foil
$N_{\mathrm{DL}}^{\mathrm{stack}}$	65732277 ± 8108	253725667 ± 15929
$N_{\mathrm{DL}}^{\mathrm{I02W15}}$	33876594 ± 5820	134144830 ± 11582
$N_{\mathrm{DL}}^{\mathrm{H09W15}}$	31855683 ± 5644	119580837 ± 10935
$\delta_{\gamma}^{\mathrm{stack}}$	0.336 ± 0.002	0.3002 ± 0.0008
$\delta_{\gamma}^{\mathrm{I02W15}}$	0.1747 ± 0.0009	0.1594 ± 0.0008
$\delta_{\gamma}^{\mathrm{H09W15}}$	0.1659 ± 0.0008	0.1452 ± 0.0007

Table 5.4 Summary of the measurements with the double sided stack.

	without foil	with foil
δ_{γ}	0.179 ± 0.009	0.159 ± 0.008
$\delta_{\gamma}^{\mathrm{HS}}$	$0.189^{+0.009}_{-0.008}$	$0.167^{+0.009}_{-0.008}$
δ_{e}	0.00146 ± 0.00007	$0.00011^{+0.000005}_{-0.00002}$
δ_{IB}	0.0189 ± 0.0006	$0.0112^{+0.0008}_{-0.0007}$

Table 5.5 Simulated values for the acceptances of detector I02W15 for the measurement with the double sided stack.

Now, as described in chapter 4 the simulation is adapted to the x and y distributions and to the detection yields of the stack. Therefore, each detector is considered individually (see sections 5.3.2 and 5.3.3).

5.3.2 Simulations and P_{KK}-result of I02W15

The simulation is adapted to the new geometry and source position of the stack. As the distances and the alignment of the source and detector are different for the measurement with the foil ($d_{\mathrm{source}}^{\mathrm{I02W15,Kapton}} = (5.1 \pm 0.3)\,\mathrm{mm}$) and without the foil ($d_{\mathrm{source}}^{\mathrm{I02W15}} = (5.3 \pm 0.3)\,\mathrm{mm}$), these detection yields are treated separately. Table 5.5 shows the yields obtained with the simulation. The error estimation is done as described in chapter 4. The errors due to different thicknesses of the foil and different distances are simulated separately and then summed up.

Figure 5.7 shows the comparison of the simulated and measured pixel X and pixel Y distributions, that were used to estimate the shift in x- and y-direction and the distance. In table 5.3.2 the simulated and measured acceptances are given. These values are in really good agreement.

As the evaluation has already been described in detail in chapter 4 and nothing unpredicted appeared, the relevant plots can be found in the appendix. Here, only the results

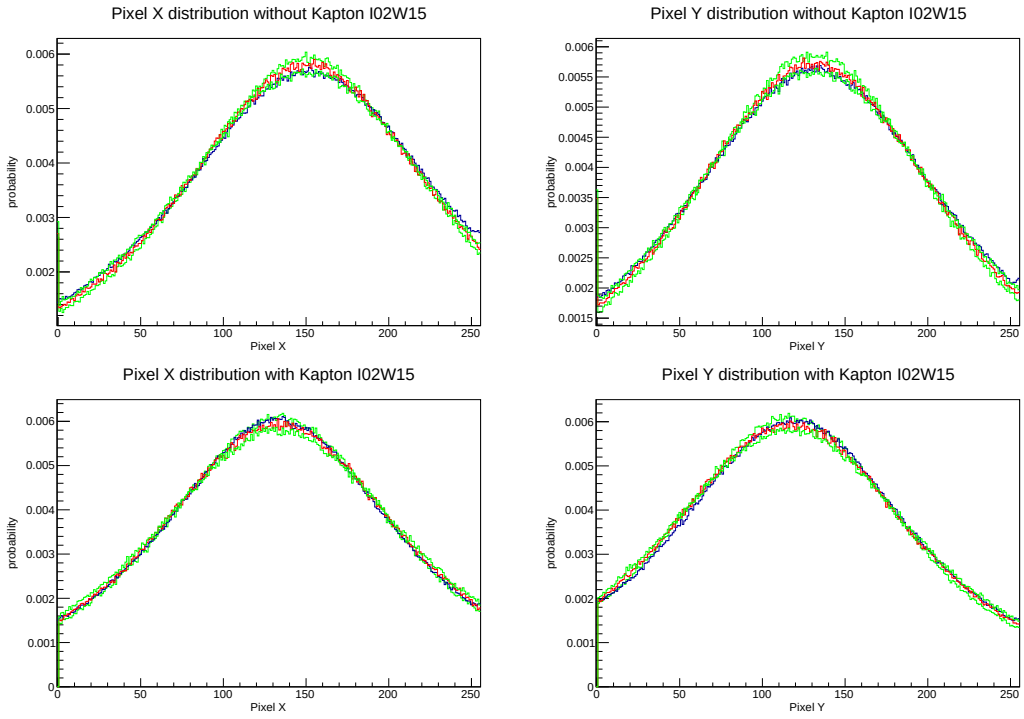

Figure 5.7 Comparison of the simulated (green, red) and measured (blue) pixel X and pixel Y distributions. The green curves show the upper and lower limits obtained by varying the distance to the detector.

of the evaluation are given (see table 5.7).

The value found here is

$$P_{\mathrm{KK}}^{\mathrm{I02W15}} = (1.775 \pm \underbrace{0.310}_{\text{stat.}} \underbrace{^{+0.061}_{-0.058}}_{\text{syst.}}) \cdot 10^{-4}. \tag{5.2}$$

	δ_γ	$\delta_\gamma^{\mathrm{Kapton}}$
simulated	0.179 ± 0.009	0.159 ± 0.008
measured	0.1731 ± 0.0009	0.1594 ± 0.0008

Table 5.6 Comparison of simulated and measured acceptances.

	with foil	without foil
$N_{\text{peak}}^{\text{meas}}$	1303 ± 191	348 ± 103
N_{DL}	134144830 ± 11582	33876594 ± 5820
P_{loss}	0.061 ± 0.005	0.064 ± 0.002
δ_γ	$0.1593^{+0.0084}_{-0.0079}$	$0.1786^{+0.0089}_{-0.0086}$
$\delta_\gamma^{\text{HS}}$	$0.1669^{+0.0090}_{-0.0072}$	$0.1835^{+0.0094}_{-0.0085}$
$\delta_{\text{e-}}$	$0.0001079^{+0.000005}_{-0.0000185}$	$0.001459^{+0.000069}_{-0.000073}$
δ_{IB}	$0.01090^{+0.0008}_{-0.0007}$	$0.01090^{+0.0008}_{-0.0007}$

Table 5.7 Summary of the simulated and measured results of I02W15.

	δ_γ	$\delta_\gamma^{\text{Kapton}}$
simulated	$0.168^{+0.009}_{-0.008}$	$0.146^{+0.008}_{-0.007}$
measured	0.1633 ± 0.0008	0.1471 ± 0.0007

Table 5.8 Comparison of simulated and measured acceptances.

5.3.3 Simulation and P_{KK}-results of H09W15

The simulation is adapted to the alignment of the detector, in order to model the result of detector H09W15. The plots obtained for the pixel distributions are shown in figure 5.8, the simulated detection yields for the fluorescence photons are compared to the measured ones in table 5.3.3. Finally, all needed values are summarized in table 5.9. The distances used were $d_{\text{source}}^{\text{H09W15,Kapton}} = (5.5 \pm 0.3)\,\text{mm}$ and $d_{\text{source}}^{\text{H09W15}} = (5.6 \pm 0.3)\,\text{mm}$. The dedicated plots are shown in the appendix.

The obtained result is

	with foil	without foil
$N_{\text{peak}}^{\text{meas}}$	750 ± 170	310 ± 97
N_{DL}	119580837 ± 10935	31855683 ± 5644
P_{loss}	0.052 ± 0.007	0.057 ± 0.004
δ_γ	$0.1459^{+0.0077}_{-0.0073}$	$0.1675^{+0.0087}_{-0.0079}$
$\delta_\gamma^{\text{HS}}$	$0.1532^{+0.0079}_{-0.0078}$	$0.1675^{+0.0087}_{-0.0079}$
$\delta_{\text{e-}}$	$0.0001061^{+0.000009}_{-0.000022}$	$0.0014229^{+0.000042}_{-0.000084}$
δ_{IB}	$0.01033^{+0.00064}_{-0.00065}$	$0.01033^{+0.00064}_{-0.00065}$

Table 5.9 Summary of the simulated and measured results of H09W15.

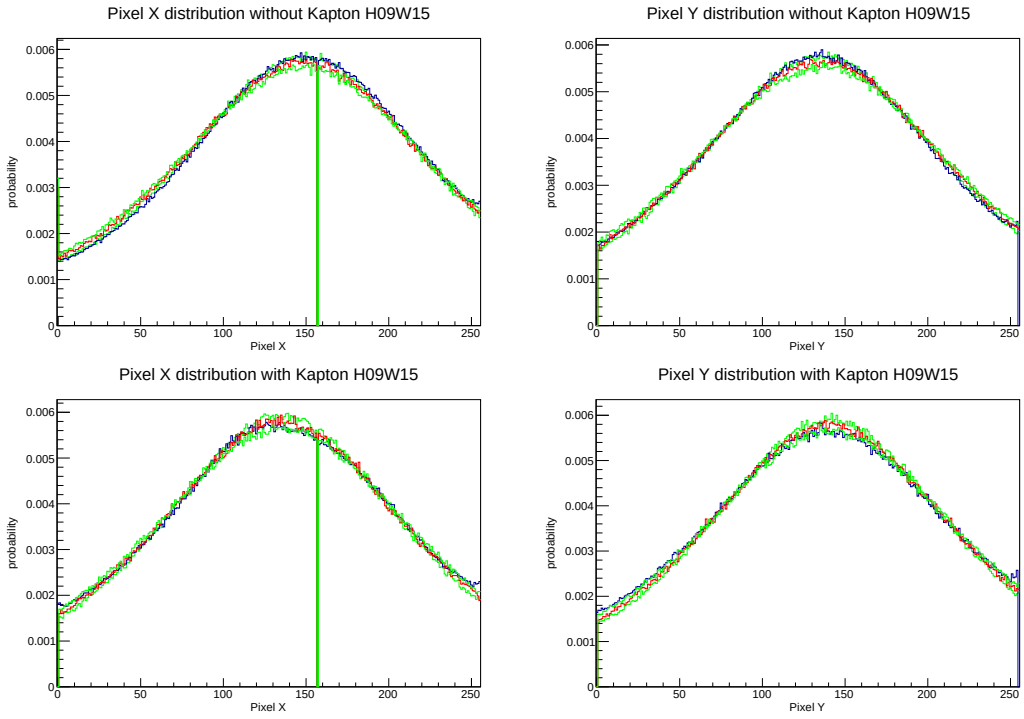

Figure 5.8 Comparison of the simulated (green, red) and measured (blue) pixel X and pixel Y distributions. The green curves show the upper and lower limits obtained by varying the distance to the detector.

$$P_{\mathrm{KK}}^{\mathrm{H09W15}} = (1.187 \pm \underbrace{0.336}_{\text{stat.}} \underbrace{^{+0.041}_{-0.038}}_{\text{syst.}}) \cdot 10^{-4}. \tag{5.3}$$

5.3.4 Results of the whole stack

As the values obtained by considering each detector individually agree quite well within the errors and the simulation is properly adapted to the experiment, the data from the whole stack is evaluated. The same procedure (clustering, and cutting on clusters with sizes smaller than three) is done as described in chapter 4, with the exception, that the two detectors are regarded as one this time. The obtained spectra of the time differences for the measurement with and without the Kapton foil are shown in figures 5.9 and 5.10.

The needed detection yields and their errors are calculated by summing up the ones for the individual detectors: $\delta_{\mathrm{i}}^{\mathrm{stack}} = \delta_{\mathrm{i}}^{\mathrm{H09W15}} + \delta_{\mathrm{i}}^{\mathrm{I02W15}}$ and conservatively $\Delta\delta_{\mathrm{i}}^{\mathrm{stack}} = \Delta\delta_{\mathrm{i}}^{\mathrm{H09W15}} + \Delta\delta_{\mathrm{i}}^{\mathrm{I02W15}}$, respectively. The results for the deteection yields, the numbers

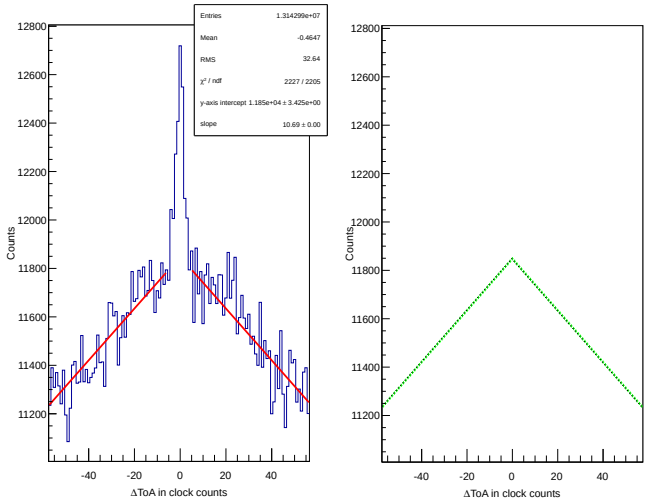

Figure 5.9 Spectrum of the time differences with Kapton foil and the fit to the background on the left. The right plot shows the extrapolation of the fit into the region of interest.

of events in the coincidence peak and the numbers of diagram line photons are given in table 5.10.

The simulation for the loss of the signal due to additional events in the subframe is performed. The plots confirming the reliability of this simulation are shown in figures 5.11, 5.12 and 5.13. In figure 5.11 the simulated and measured time spectra, and in figures 5.12 and 5.13 the distributions of the number of hits per frame, are compared. Again, a good agreement between simulation and measurement can be seen. The value for the loss is also given in table 5.11.

The distribution of the P_{KK}-values obtained by generating random numbers according to the uncertainties can be seen in figure 5.14.

Finally, this leads to

$$P_{\mathrm{KK}} = (1.400 \pm \underbrace{0.165}_{\text{stat.}} \underbrace{^{+0.048}_{-0.045}}_{\text{syst.}}) \cdot 10^{-4}. \tag{5.4}$$

This value is in good agreement with the values obtained by previous experiments (see section 2.1). As the statistical error of the measurement with the Kapton foil is the limiting factor, more measuring time is needed to decrease the statistical uncertainty of

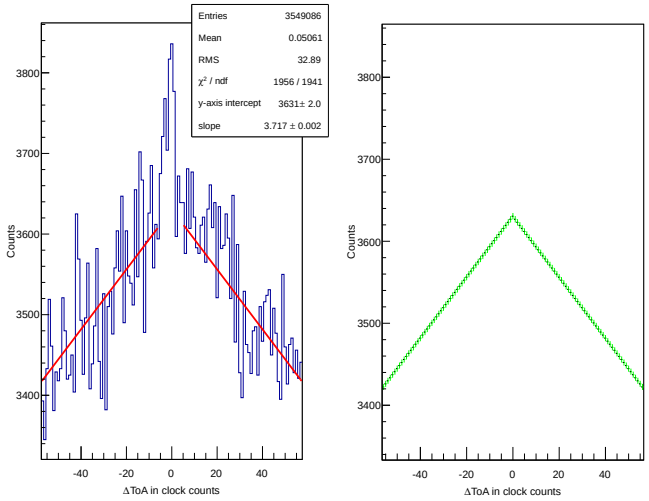

Figure 5.10 Spectrum of the time differences without Kapton foil and the fit to the background on the left. The right plot shows the extrapolation of the fit into the region of interest.

the P_{KK} value.

The obtained result does not favor any of the theoretical P_{KK}-value shown in figure 2.4, but excludes the two highest ones $P_{\mathrm{KK}}^{\mathrm{theo}} = 4.8 \cdot 10^{-4}$ with a significance of 16σ and $P_{\mathrm{KK}}^{\mathrm{theo}} = 2.4 \cdot 10^{-4}$ on a 4σ-level.

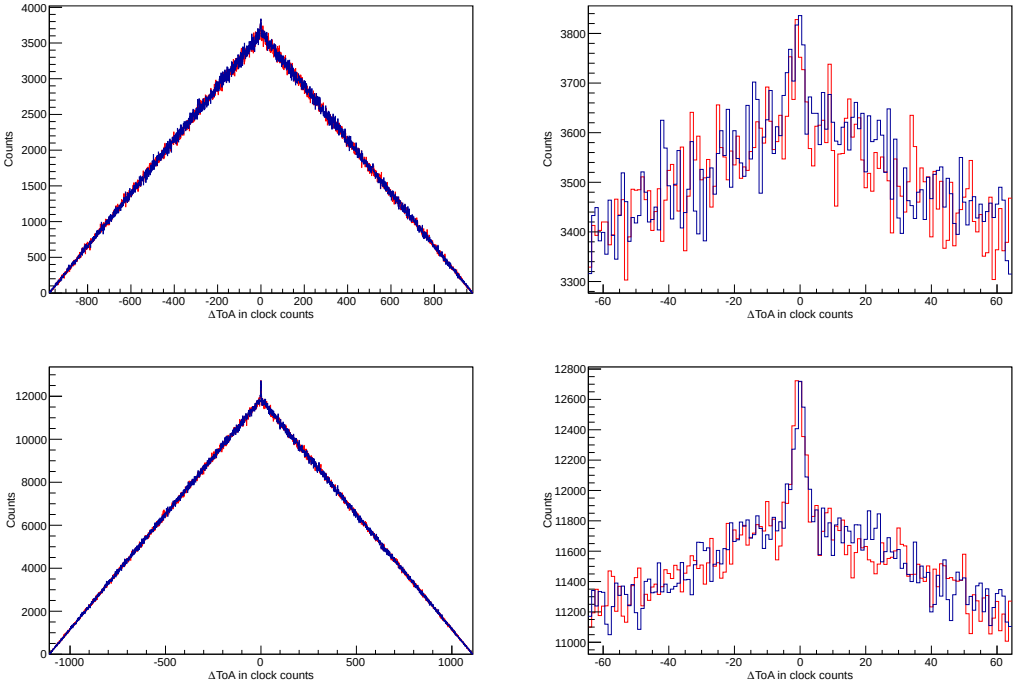

Figure 5.11 Comparison of the simulated (red) and measured spectra (blue) for the setup without (upper plots) and with the Kapton foil (lower plots).

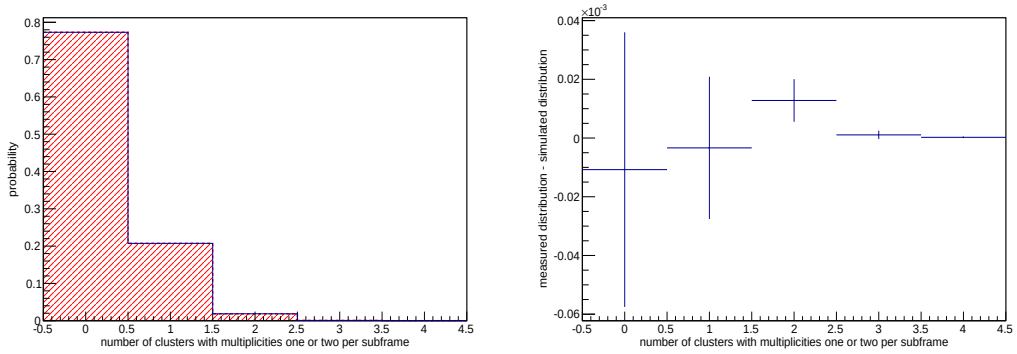

Figure 5.12 Simulated (red) and measured (blue) distributions of the number of hits in one subframe with the Kapton foil (on the left) and the difference of these distributions (right) for the measurement with the Kapton foil.

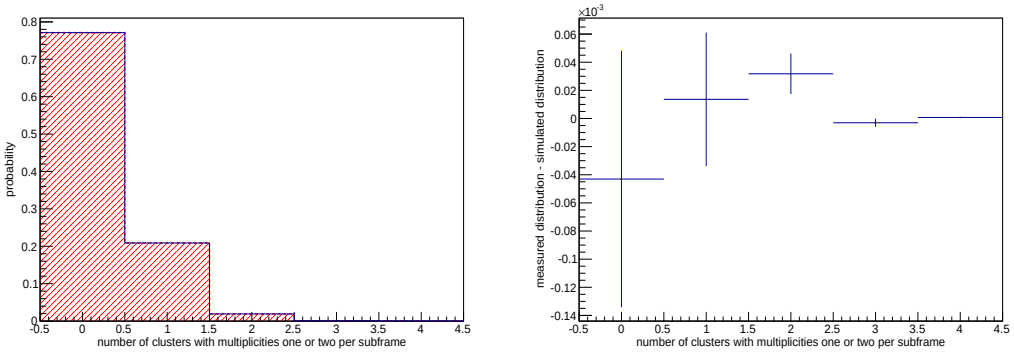

Figure 5.13 Simulated (red) and measured (blue) distributions of the number of hits in one subframe with the Kapton foil (on the left) and the difference of these distributions (right) for the measurement without the Kapton foil.

	with foil	without foil
$N_{\text{peak}}^{\text{meas}}$	3428 ± 349	999 ± 193
N_{DL}	253725667 ± 15929	65732277 ± 8108
P_{loss}	0.116 ± 0.004	0.111 ± 0.004
δ_{γ}	$0.305^{+0.016}_{-0.015}$	0.346 ± 0.017
$\delta_{\gamma}^{\text{HS}}$	$0.351^{+0.017}_{-0.021}$	$0.320^{+0.018}_{-0.021}$
$\delta_{\text{e-}}$	$0.000214^{+0.000014}_{-0.000041}$	$0.00288^{+0.00011}_{-0.00016}$
δ_{IB}	0.0215 ± 0.0013	0.0215 ± 0.0013

Table 5.10 Summary of simulated and measured results from the whole double sided stack.

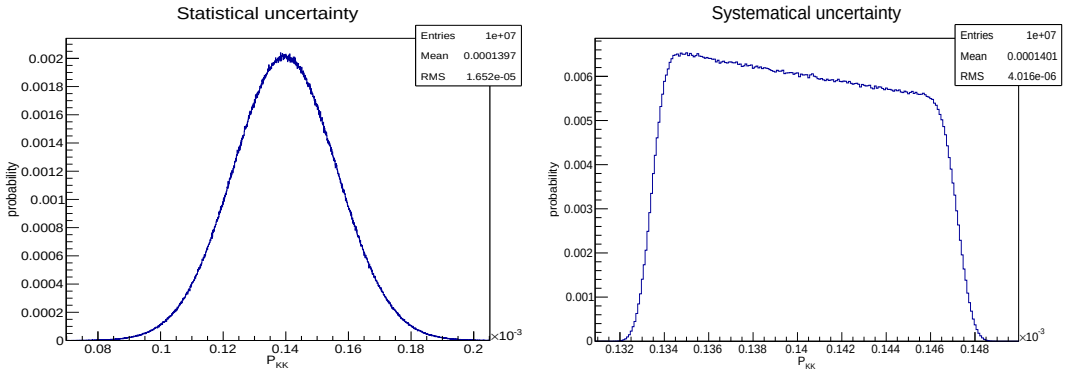

Figure 5.14 Distribution of the P_{KK}-values taking into account the statistical errors (left) and the systematical ones (right).

6 First results on the angular correlation between hypersatellite and satellite momenta

Contents

6.1 Data evaluation and simulation

One goal of this work is to search for an angular correlation between the two coincidently emitted fluorescence photons. Because of their pixelisation Timepix devices are appropriate tools for this investigation. Therefore, the data from the double sided stack with the Kapton foil is considered, as, in this data, the electronic contribution is lowered to a fraction $\frac{N_e^{\text{Kapton}}}{N_e} = \frac{\delta_e^{\text{Kapton}}}{\delta_e} \approx 0.07$. In the evaluation, first the clustering is done, a cut is made on clusters with multiplicities one or two, the division into subframes and at last the cut on subframes containing exactly two clusters with multiplicities one or two, is applied. Now, the main information is not only ToA but also the coordinates of the pixel hit and the time difference between the two events.

First one has to define a common coordinate system for both detectors. Here the center of the source is taken as the origin. For the coordinates the actual positions of the detectors with respect to the origin have to be adjusted. The z positions are given by the distances from the detectors to the source (see chapter 5), where detector I02W15 has a negative z-value as it is "below" the source. The adjustment of the x- and y-positions is done using the mean values of the appropriate distributions. As detector H09W15 is rotated by 180° around the x-axis, the x- and y-values are calculated by $x^{\text{rel}}_{\text{H09W15}}(x) = x^0_{\text{H09W15}} - x$, respectively $y^{\text{rel}}_{\text{H09W15}}(y) = y^0_{\text{H09W15}} - y$. The adjustment is then the problem of the determination of the y^0_i and x^0_i, so that four equations have to be solved:

Detector	x^0 in pixel	y^0 in pixel	z^0 in pixel
I02W15	-131	-122	-96
H09W15	132	133	101

Table 6.1 Relative positions of the detectors with respect to the center of the source in pixel.

$$\begin{cases} x^{\mathrm{rel}}_{\mathrm{H09W15}}(x_{\mathrm{mean}}) & = x^0_{\mathrm{H09W15}} - x_{\mathrm{mean}} = 0, \\ y^{\mathrm{rel}}_{\mathrm{H09W15}}(y_{\mathrm{mean}}) & = y^0_{\mathrm{H09W15}} - y_{\mathrm{mean}} = 0, \\ x^{\mathrm{rel}}_{\mathrm{I02W15}}(x_{\mathrm{mean}}) & = x^0_{\mathrm{I02W15}} + x_{\mathrm{mean}} = 0, \\ y^{\mathrm{rel}}_{\mathrm{I02W15}}(y_{\mathrm{mean}}) & = y^0_{\mathrm{I02W15}} + y_{\mathrm{mean}} = 0. \end{cases} \tag{6.1}$$

Table 6.1 shows the calculated values. One can define two vectors $\vec{a} = (x^{\mathrm{rel}}_{\mathrm{I02W15}}, y^{\mathrm{rel}}_{\mathrm{I02W15}}, z^{\mathrm{rel}}_{\mathrm{I02W15}})^{\mathrm{T}}$ and $\vec{b} = (x^{\mathrm{rel}}_{\mathrm{H09W15}}, y^{\mathrm{rel}}_{\mathrm{H09W15}}, z^{\mathrm{rel}}_{\mathrm{H09W15}})^{\mathrm{T}}$ and the angle between these vectors is calculated as

$$\vec{a} \cdot \vec{b} = |a| \cdot |b| \cdot \cos\alpha \rightarrow \alpha = \arccos \frac{\vec{a} \cdot \vec{b}}{|a| \cdot |b|}. \tag{6.2}$$

For the further evaluation each calculated angle is stored with the corresponding coordinates and the time difference between the two coincident events in a TTree (see [19]). Thus, cuts on the time differences can easily be applied.

As the radioactive source used is no real point source, this data has to be compared to the simulation. For this task the ROSI package is used again: Two particles are emitted at the same time and the simulated x and y positions are written to ASCII files. The same evaluation as for the measured data is performed. As there are two types of coincident events, the random coincidences, where the two photons have different origins and the true coincidences, where the photons have the same origin, these contributions have to be simulated separately. To get an impression of the reliability of the simulated data, the simulated angular distribution for the randoms is compared to the measured one (see figure 6.1). To get rid of the true coincidences in the measurement for the comparison, only those angles are taken, where the time differences between the events is bigger than 4 or smaller than -5 clock counts. Each angular distribution is normalized using the condition $\Sigma_{\mathrm{i}} h_{\mathrm{i}} = 1$.

These distributions are in good agreement. Wherefore in the next section an attempt is made to find an angular dependence for the coincident hypersatellite satellite emission.

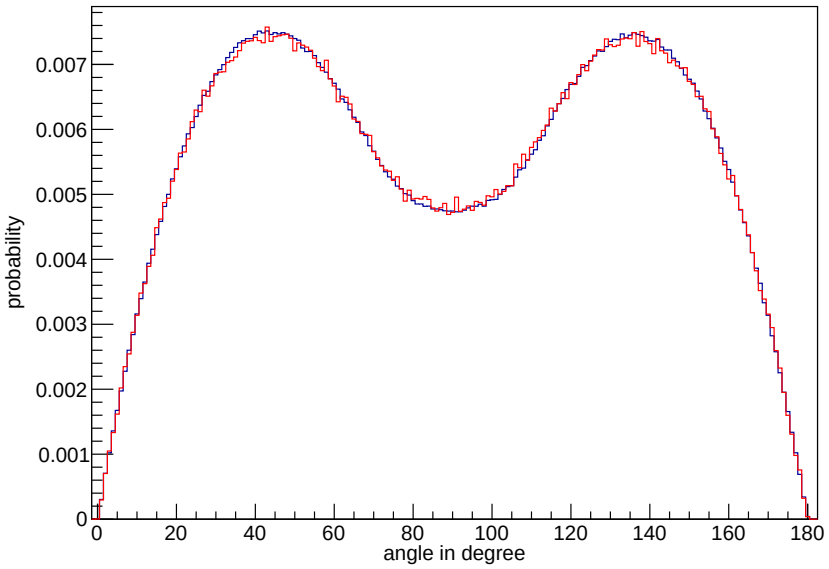

Figure 6.1 Comparison of the measured (blue) and simulated (red) angular distributions for the random coincident background.

6.2 Angular distribution

As next, the angular distribution of the true coincidences is investigated. Therefore all angles with time differences in the interval $[-5; 4]$ clock counts are considered and filled into a histogram. This distribution contains the random background events as well as the true coincident ones:

$$f_{\text{coincident}}(\Delta\text{ToA}) = f_{\text{random}}(\Delta\text{ToA}) + f_{\text{true}}(\Delta\text{ToA}). \tag{6.3}$$

To get the angular distribution of the events in the coincidence peak the distribution of the random coincidences (see figure 6.1) is subtracted from the measured coincident one. Therefore, these histograms have to be scaled by the relevant integrals of the fitted curve (see figure 5.9, right side), i.e. $\frac{1}{\int_{-5}^{4} f_{\text{fit}}}$ for the distribution in the signal range and $\frac{1}{\int_{-1109}^{-6} f_{\text{fit}} + \int_{5}^{1109} f_{\text{fit}}}$ for the distribution of the random events, respectively. These scaled distributions and the resulting one for the true coincidences are shown in figure 6.2. [1]

[1] Consistently, the same upper and lower limits for the coincident region as in chapter 5 were used.

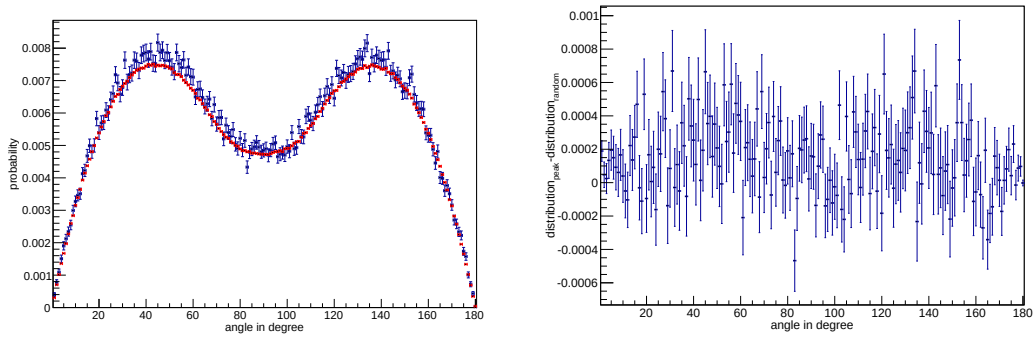

Figure 6.2 Comparison of the scaled angular spectra of the randoms and the coincident ones (left) and the one obtained by subtracting the random spectrum from the coincident one (right).

To see if there is an angular dependence of this coincident emission, this distribution has to be corrected for the angular dependence of the solid angle acceptance. Therefore the simulation is used, where two coincident particles are isotropically emitted. The simulated angular distribution is shown in figure 6.3.

The correction of the measured data is done by dividing the bin contents of the measured by the contents of the simulated histogram. The resulting one is shown in figure 6.4) and shows a flat distribution with a sharp peak in the bin with angles $\Theta \in [0.5; 1.5[$.

This "small angle peak" may not just be caused by a possible angular correlation of the hypersatellite satellite momenta, but also by tracks on the pixel matrix interrupted by masked pixels. This possibility is investigated in the following: The relative coordinates on the matrix of the two coincident events are compared to the map of the masked pixels for both detectors (see figure 6.5). For detector H09W15 six events were found that may be due to such interrupted tracks. [2] Doing the same evaluation as described above, taking out these six events, one finds the histogram shown in figure 6.6. This histogram is rebinned by a factor of four and shown in figure 6.7.

Still, this "small angle" feature can be seen in the distribution and should be a topic of further investigations. But, as this deviation is not significant, with the actual evaluation and the statistic up to now no evidence for an angular distribution can be found.

At last, a few notes on this preliminary angular distribution shall be made:

[2] Please note: This coincidences caused by interrupted tracks also have to be considered in the future high precision P_{KK}-evaluation (see chapter 5). With the actual evaluation these six events are negligible compared to the number of coincident events ($N_{\mathrm{peak}}^{\mathrm{meas}} = 3428$).

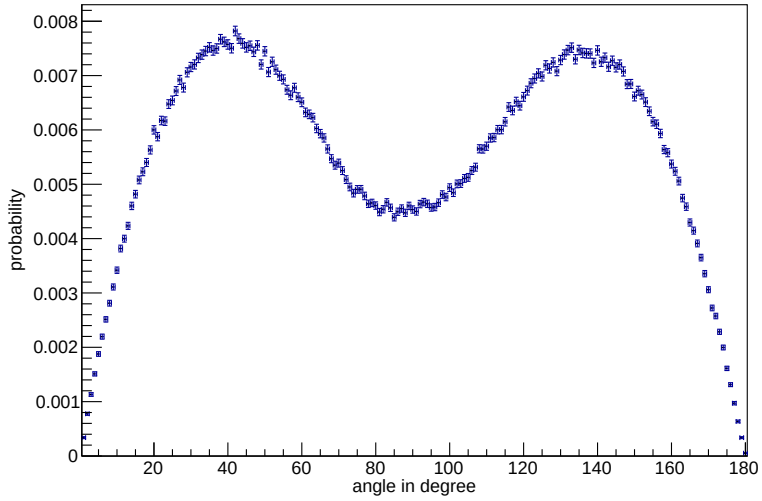

Figure 6.3 Simulated angular distribution of the true coincidences.

- This angular distribution contains all possible coincident events described in chapter 3, i.e. $\gamma_{\mathrm{HS}}\,\gamma\,\overline{\mathrm{e}\text{-}}$, $\overline{\gamma_{\mathrm{HS}}}\,\gamma\,\mathrm{e}\text{-}$, $\gamma_{\mathrm{HS}}\,\overline{\gamma}\,\mathrm{e}\text{-}$, $\gamma_{\mathrm{HS}}\,(1-\gamma)\,\mathrm{e}\text{-}$, $(1-\gamma_{\mathrm{HS}})\,\gamma\,\mathrm{e}\text{-}$, as well as the coincidences of internal Bremsstrahlung photons or electrons from the L- and M-shell with K-fluorescences. As only the hypersatellite satellite coincidence emission $\gamma_{\mathrm{HS}}\,\gamma\,\overline{\mathrm{e}\text{-}}$ is the signal of interest, its contribution $P_{\gamma_{\mathrm{HS}},\gamma,\overline{\mathrm{e}\text{-}}}$ to the distribution is estimated using the formula

$$\begin{aligned} 1 =& \frac{N_{\mathrm{DL}}^{\mathrm{Kapton}}}{N_{\mathrm{peak}}^{\mathrm{coinc,Kapton}}} \cdot (P_{\mathrm{KK}} \cdot [\delta_{\gamma}^{\mathrm{HS}}(1-\delta_{\mathrm{e}\text{-}})\omega_{K_{\alpha,\beta}} + (1-\delta_{\gamma}^{\mathrm{HS}})\delta_{\mathrm{e}\text{-}}\omega_{K_{\alpha,\beta}} \\ &+ \frac{\delta_{\gamma}^{\mathrm{HS}}}{\delta_{\gamma}}(1-\delta_{\gamma})\delta_{\mathrm{e}\text{-}}\omega_{K_{\alpha,\beta}} + \frac{\delta_{\gamma}^{\mathrm{HS}}}{\delta_{\gamma}}\delta_{\mathrm{e}\text{-}}(1-\omega_{K_{\alpha,\beta}}) + \delta_{\mathrm{e}\text{-}}(1-\omega_{K_{\alpha,\beta}})] \\ &+ P_{\mathrm{e}\text{-}}\delta_{\mathrm{e}\text{-}} + P_{\mathrm{IB}}\delta_{IB}), \end{aligned} \tag{6.4}$$

derived from the formulae given in chapter 3. With the values given in table 5.10 for the measurement with the Kapton foil and the result of the P_{KK}-evaluation, one finds:

$$P_{\gamma_{\mathrm{HS}},\gamma,\overline{\mathrm{e}\text{-}}} = \frac{P_{\mathrm{KK}} \cdot \delta_{\gamma}^{\mathrm{HS}} \cdot (1-\delta_{\mathrm{e}}) \cdot \omega_{K_{\alpha,\beta}} \cdot N_{\mathrm{DL}}^{\mathrm{Kapton}}}{N_{\mathrm{peak}}^{\mathrm{coinc,Kapton}}} = 0.942 = 94.2\%. \tag{6.5}$$

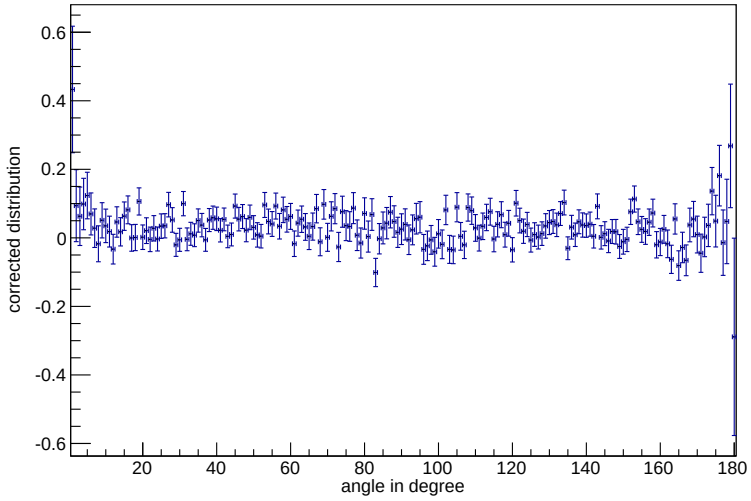

Figure 6.4 Corrected angular distribution for the true coincidences.

This means that 94.2% of all events used for the determination of the angular correlation function were due to hypersatellite satellite coincidences.

- The measured distribution $f_{\text{meas}}(\Theta)$ is a convolution of the distribution of the "true" emitted angles $f_{\text{true}}(\Theta)$ with the response function of the detector $R(\Theta)$:

$$f_{\text{meas}}(\Theta) = f_{\text{true}}(\Theta) \otimes R(\Theta). \tag{6.6}$$

  Thus, to get the true angular spectrum the response of the detector to the different angles between the fluorescence photons has to be simulated to perform a deconvolution of the measured distribution.

- The errorbars shown in the plots do not include any systematical uncertainty due to the uncertainty of the distances of the detectors to the source and the thickness of the Kapton foil. Their estimation can be done in the same way as described in chapter 5.

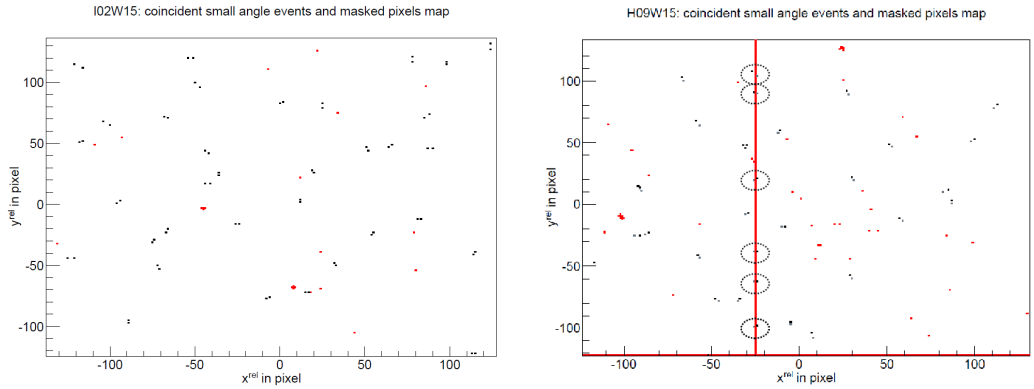

Figure 6.5 Coincident small angle events on the pixel matrix for the detectors I02W15 (left) and H09W15 (right). The relative coordinates of this events (black) are compared to the map of masked pixels (red). In this way six coincident events were found for detector H09W15 that may be due to interrupted tracks (see circles).

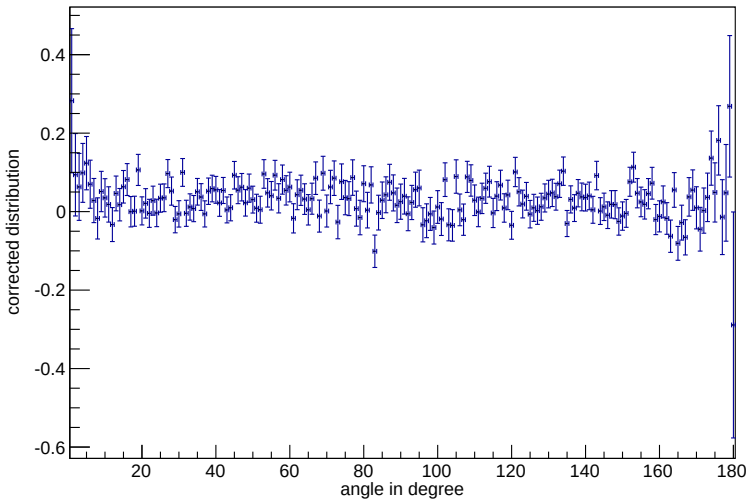

Figure 6.6 Corrected angular distribution: Interrupted tracks were taken out of the evaluation.

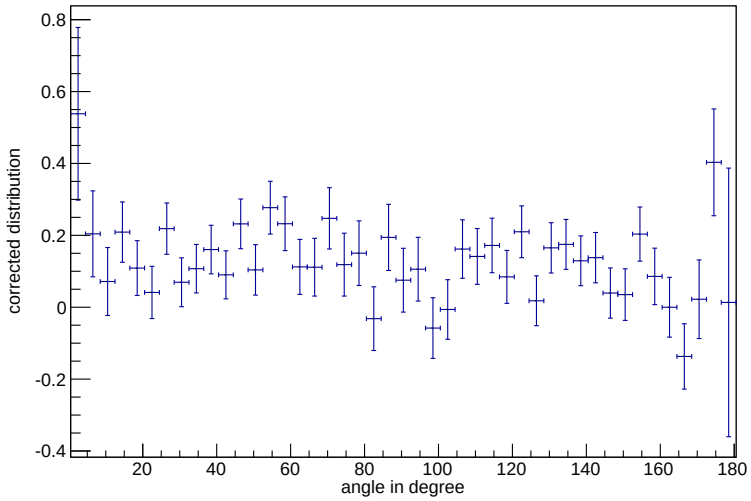

Figure 6.7 Rebinned corrected angular distribution: Interrupted tracks weren taken out of the evaluation.

7 Summary and outlook

The main goals of this work were achieved. It was shown that with a stack consisting of two Timepix devices the current uncertainties of the P_{KK}-value of the isotope ^{55}Fe can be decreased by at least a factor of two within reasonable measuring time, even without having any energy information. The result obtained in this work is

$$P_{\mathrm{KK}} = 1.400 \underbrace{\pm 0.165}_{\text{stat.}} \underbrace{^{+0.048}_{-0.045}}_{\text{syst.}} \cdot$$

Simultaneously, for the first time the angular correlation function for the coincident hypersatellite satellite emission was presented. For a statement on an angular correlation further investigations, like simulating the angular response function of the detector and estimating the systematic error of the setup used, and data with more statistics are needed.

The presented evaluation contains about 73 days of measurement with the Kapton foil, which corresponds to an effective measuring time $t_{\mathrm{eff}}^{\mathrm{Kapton}} = 14\,\mathrm{h}$ (and about 20 days without the Kapton foil corresponding to $t_{\mathrm{eff}} = 3\,\mathrm{h}$). As the error is dominated by the error on the number of measured coincident events with the Kapton foil, only this measurement has to be extended by a factor of three (meaning about 220 days of measuring) in order to decrease the statistical error to $\Delta P_{\mathrm{KK}} = 0.095 \cdot 10^{-4}$, get the result with the lowest uncertainty and being able to favor a theoretical model.

Faster readouts as well as detectors which can provide energy- and time of arrival information simultaneously are being developed which could speed up the measurements remarkably. Thus, the described measurements and evaluation can be done for different elements to prove the Z-dependency of the P_{KK}-value and search for an angular correlation of the coincident hypersatellite satellite emission. In the pure LS-coupling of the low Z elements, like iron, which was investigated in this work, the spin-flip transition is forbidden. As with increasing atomic number Z jj-coupling becomes more dominant, those elements may show other features in their angular correlation functions.

A Detailed drawings of the holders

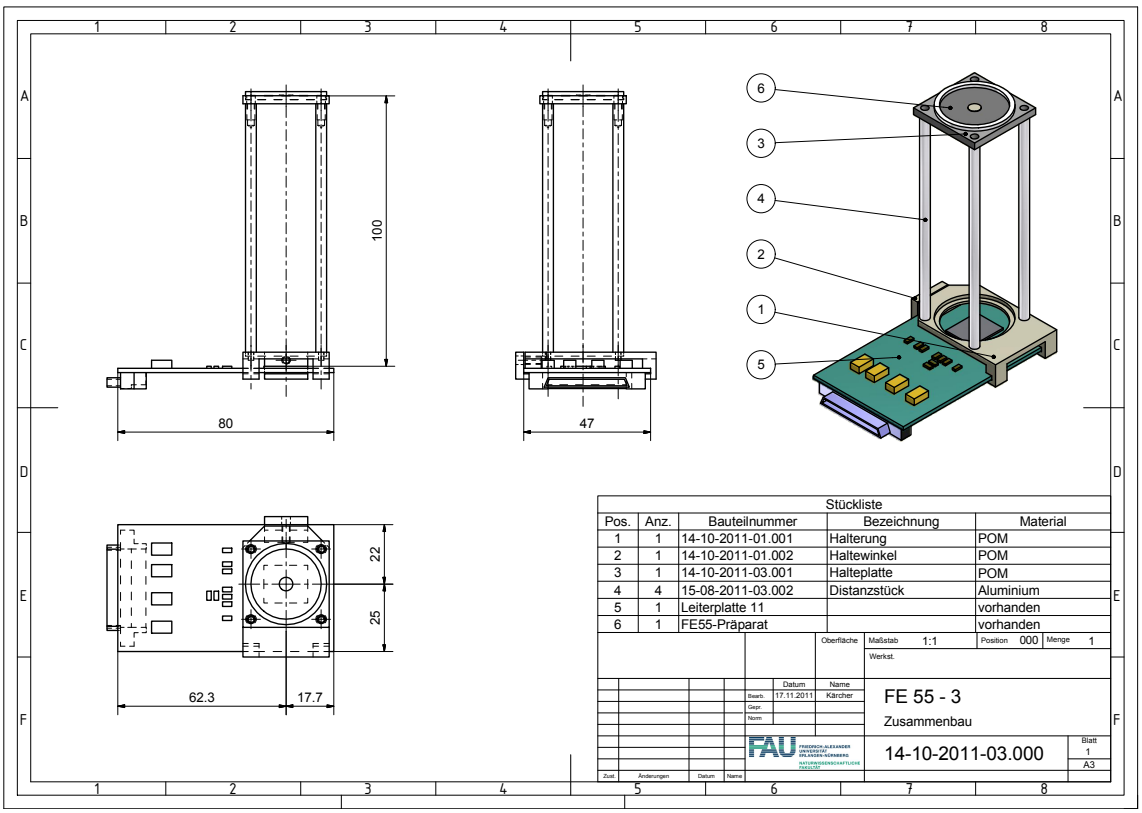

Figure A.1 Detailed drawing of the holder for the ^{55}Fe source used for the measurement of the detection efficiency. The distances are given in mm. As the modeled timepix-device was not bump bonded to a sensor layer, the actual distance from the top of the sensor layer to the source is 0.3 mm smaller.

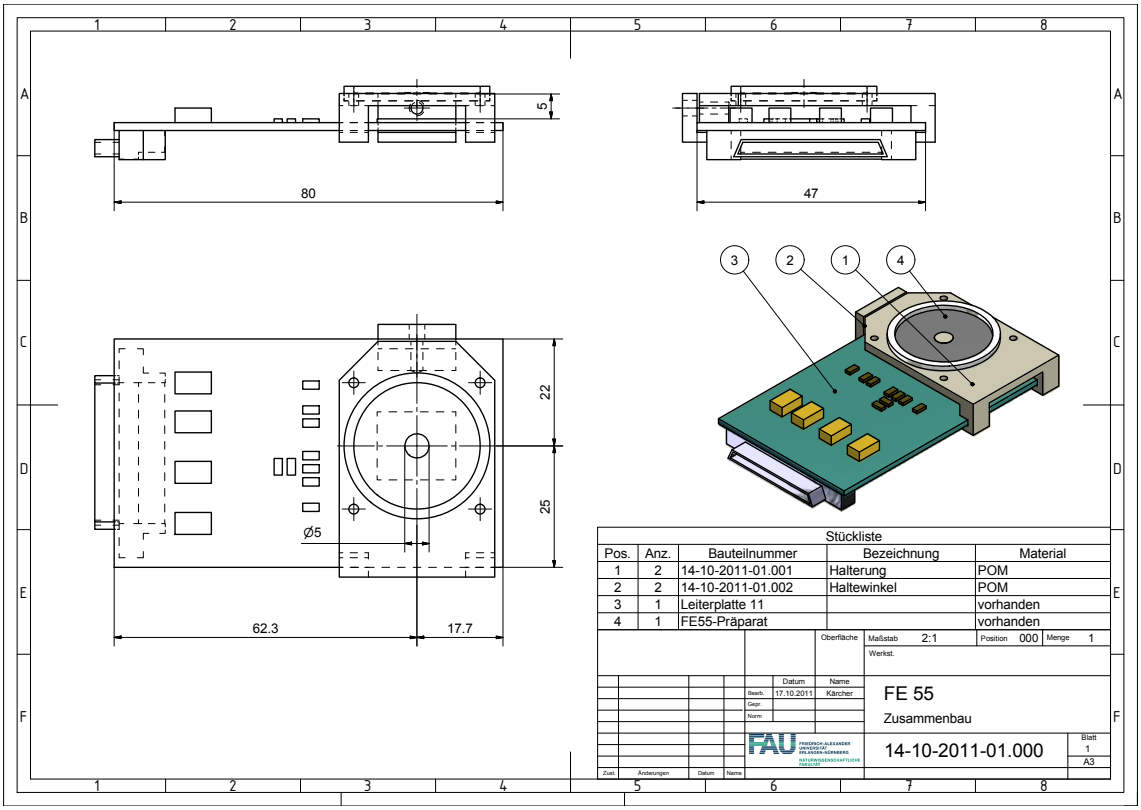

Figure A.2 Detailed drawing of the one sided readout stack for the ^{55}Fe source. The distances are given in mm. As the modeled timepix-device was not bump bonded to a sensor layer, the actual distance from the top of the sensor layer to the source is 0.3 mm smaller.

B Tables

Date	$A(t)$ in kBq	t_{eff} in s	$N_{\text{DL}}^{\text{stack}}$	$N_{\text{DL}}^{\text{I02W15}}$	$N_{\text{DL}}^{\text{H09W15}}$
17/02/2012	63.11 ± 0.96	1345.4	8311956 ± 2883	4439979 ± 2107	3875819 ± 1969
22/02/2012	62.90 ± 0.95	1345.4	8246390 ± 2872	4421673 ± 2103	3828649 ± 1957
24/02/2012	62.81 ± 0.95	1345.4	8228450 ± 2869	4491930 ± 2119	3740853 ± 1934
27/02/2012	62.66 ± 0.95	886.8	5349956 ± 2313	2909906 ± 1706	2442935 ± 1563
02/03/2012	62.50 ± 0.95	1345.4	7968664 ± 2823	3947053 ± 1987	4024977 ± 2006
05/03/2012	62.38 ± 0.95	1345.4	7940193 ± 2818	3929574 ± 1982	4014059 ± 2004
07/03/2012	62.30 ± 0.95	1345.4	7901672 ± 2811	3913763 ± 1978	3991399 ± 1998
09/03/2012	62.20 ± 0.94	1345.4	7905301 ± 2812	3909475 ± 1977	3999305 ± 2000
11/03/2012	62.11 ± 0.94	682.4	3913605 ± 1978	1913835 ± 1383	2001443 ± 1415

Table B.1 Measurements with the double sided stack without the Kapton foil: The dates, the appropriate activities of the ^{55}Fe source and the measured numbers of diagram line photons.

Date	$\delta_\gamma^{\text{stack}}$	$\delta_\gamma^{\text{I02W15}}$	$\delta_\gamma^{\text{H09W15}}$
17/02/2012	0.345 ± 0.005	0.185 ± 0.003	0.164 ± 0.002
22/02/2012	0.343 ± 0.005	0.186 ± 0.003	0.162 ± 0.002
24/02/2012	0.343 ± 0.005	0.189 ± 0.003	0.159 ± 0.002
27/02/2012	0.339 ± 0.005	0.186 ± 0.003	0.158 ± 0.002
02/03/2012	0.334 ± 0.005	0.167 ± 0.003	0.171 ± 0.003
05/03/2012	0.333 ± 0.005	0.166 ± 0.003	0.171 ± 0.003
07/03/2012	0.332 ± 0.005	0.166 ± 0.003	0.170 ± 0.003
09/03/2012	0.333 ± 0.005	0.161 ± 0.002	0.171 ± 0.003
11/03/2012	0.325 ± 0.005	0.166 ± 0.003	0.169 ± 0.003

Table B.2 Calculated acceptances for the measurements without the foil.

Run number	$A(t)$ in kBq	$N_{\mathrm{DL}}^{\mathrm{stack}}$	$N_{\mathrm{DL}}^{\mathrm{I02W15}}$	$N_{\mathrm{DL}}^{\mathrm{H09W15}}$
7	60.51 ± 0.92	7893319 ± 2810	4165399 ± 2041	3727920 ± 1931
8	60.42 ± 0.92	7878467 ± 2807	4148646 ± 2037	3729821 ± 1931
9	60.33 ± 0.92	7844157 ± 2801	4135584 ± 2034	3708573 ± 1926
10	60.24 ± 0.91	7826070 ± 2798	4130711 ± 2032	3695359 ± 1922
11	60.15 ± 0.91	7839362 ± 2800	4132220 ± 2033	3707142 ± 1925
12	60.06 ± 0.91	7828812 ± 2798	4120305 ± 2030	3708507 ± 1926
13	59.97 ± 0.91	7804376 ± 2794	4114963 ± 2029	3689413 ± 1921
14	59.88 ± 0.91	7812065 ± 2795	4119274 ± 2030	3692791 ± 1922
15	59.80 ± 0.91	7788395 ± 2791	4123522 ± 2031	3664873 ± 1914
16	59.71 ± 0.91	7779004 ± 2789	4123633 ± 2031	3655371 ± 1912
17	59.62 ± 0.90	7748915 ± 2784	4103953 ± 2026	3644962 ± 1909
18	59.53 ± 0.90	7713061 ± 2777	4082834 ± 2021	3630227 ± 1905
19	59.45 ± 0.90	7706412 ± 2776	4088017 ± 2022	3618395 ± 1902
20	59.35 ± 0.90	7721487 ± 2779	4099002 ± 2025	3622485 ± 1903
21	59.27 ± 0.90	7738456 ± 2782	4101075 ± 2025	3637381 ± 1907
22	59.18 ± 0.90	7731870 ± 2781	4079366 ± 2020	3652504 ± 1911
23	59.09 ± 0.90	7665386 ± 2769	4073346 ± 2018	3592040 ± 1895
24	59.00 ± 0.90	7655807 ± 2767	4051631 ± 2013	3604176 ± 1898
25	58.92 ± 0.89	7651644 ± 2766	4046328 ± 2012	3605316 ± 1899
26	58.83 ± 0.89	7653421 ± 2766	4054162 ± 2013	3599259 ± 1897
27	58.74 ± 0.89	7641827 ± 2764	4044106 ± 2011	3597721 ± 1897
28	58.65 ± 0.89	7627520 ± 2762	4020535 ± 2005	3606985 ± 1899
29	58.57 ± 0.89	7617466 ± 2760	4012038 ± 2003	3605428 ± 1899
30	58.48 ± 0.89	7608600 ± 2758	4030751 ± 2008	3577849 ± 1892
31	58.39 ± 0.89	7593957 ± 2756	4010250 ± 2003	3583707 ± 1893
32	58.30 ± 0.88	7584504 ± 2754	4022044 ± 2006	3562460 ± 1887
33	58.10 ± 0.88	7589079 ± 2755	3995895 ± 1999	3593184 ± 1896
34	58.02 ± 0.88	7573046 ± 2752	3998005 ± 2000	3575041 ± 1891
35	57.94 ± 0.88	7545006 ± 2747	4000067 ± 2000	3544939 ± 1883
36	57.86 ± 0.88	7534368 ± 2745	3991979 ± 1998	3542389 ± 1882
37	57.77 ± 0.88	7526891 ± 2744	3981219 ± 1995	3545672 ± 1883
38	57.69 ± 0.88	7529864 ± 2744	3986022 ± 1997	3543842 ± 1883
39	57.61 ± 0.87	7473053 ± 2734	3957948 ± 1989	3515105 ± 1875

Table B.3 Measurement with the Kapton foil. The data was divided into run containing of 661 repetitions, each with 10000 frames.

Run number	$\delta_\gamma^{\text{stack}}$	$\delta_\gamma^{\text{I02W15}}$	$\delta_\gamma^{\text{H09W15}}$
7	0.301 ± 0.005	0.1587 ± 0.0024	0.1421 ± 0.0022
8	0.301 ± 0.005	0.1583 ± 0.0024	0.1423 ± 0.0022
9	0.300 ± 0.005	0.1581 ± 0.0024	0.1417 ± 0.0022
10	0.300 ± 0.005	0.1581 ± 0.0024	0.1414 ± 0.0021
11	0.300 ± 0.005	0.1584 ± 0.0024	0.1421 ± 0.0022
12	0.301 ± 0.005	0.1582 ± 0.0024	0.1424 ± 0.0022
13	0.300 ± 0.005	0.1582 ± 0.0024	0.1418 ± 0.0022
14	0.301 ± 0.005	0.1586 ± 0.0024	0.1422 ± 0.0022
15	0.300 ± 0.005	0.1590 ± 0.0024	0.1413 ± 0.0021
16	0.300 ± 0.005	0.1592 ± 0.0024	0.1412 ± 0.0021
17	0.300 ± 0.005	0.1587 ± 0.0024	0.1410 ± 0.0021
18	0.299 ± 0.005	0.1581 ± 0.0024	0.1406 ± 0.0021
19	0.299 ± 0.005	0.1586 ± 0.0024	0.1403 ± 0.0021
20	0.300 ± 0.005	0.1592 ± 0.0024	0.1407 ± 0.0021
21	0.301 ± 0.005	0.1595 ± 0.0024	0.1415 ± 0.0021
22	0.301 ± 0.005	0.1589 ± 0.0024	0.1423 ± 0.0022
23	0.299 ± 0.005	0.1589 ± 0.0024	0.1402 ± 0.0021
24	0.299 ± 0.005	0.1583 ± 0.0024	0.1408 ± 0.0021
25	0.299 ± 0.005	0.1583 ± 0.0024	0.1411 ± 0.0021
26	0.300 ± 0.005	0.1589 ± 0.0024	0.1411 ± 0.0021
27	0.300 ± 0.005	0.1587 ± 0.0024	0.1412 ± 0.0021
28	0.300 ± 0.005	0.1580 ± 0.0024	0.1418 ± 0.0022
29	0.300 ± 0.005	0.1579 ± 0.0024	0.1419 ± 0.0022
30	0.300 ± 0.005	0.1589 ± 0.0024	0.1411 ± 0.0021
31	0.300 ± 0.005	0.1583 ± 0.0024	0.1415 ± 0.0021
32	0.300 ± 0.005	0.1591 ± 0.0024	0.1409 ± 0.0021
33	0.301 ± 0.005	0.1586 ± 0.0024	0.1426 ± 0.0022
34	0.301 ± 0.005	0.1589 ± 0.0024	0.1421 ± 0.0022
35	0.300 ± 0.005	0.1592 ± 0.0024	0.1411 ± 0.0021
36	0.300 ± 0.005	0.1591 ± 0.0024	0.1412 ± 0.0021
37	0.300 ± 0.005	0.1589 ± 0.0024	0.1415 ± 0.0021
38	0.301 ± 0.005	0.1593 ± 0.0024	0.1416 ± 0.0022
39	0.299 ± 0.005	0.1584 ± 0.0024	0.1407 ± 0.0021

Table B.4 Calculated acceptances for the measurements with the foil.

C Plots of the P_{KK}-evaluation for I02W15

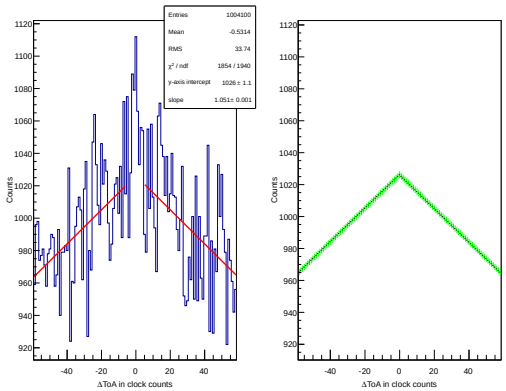

Figure C.1 Spectrum of time differences without the foil with the fit to the background on the left and extrapolation of the fit on the right. The detector is I02W15.

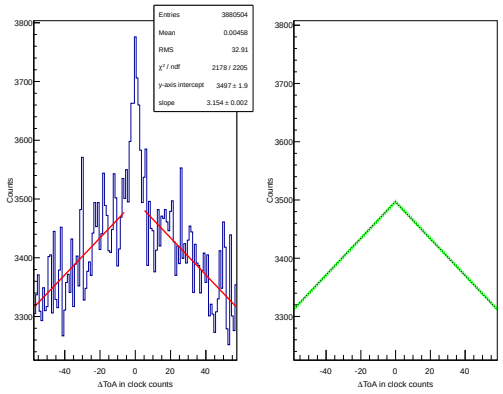

Figure C.2 Spectrum of time differences with the foil with the fit to the background on the left and extrapolation of the fit on the right. The detector is I02W15.

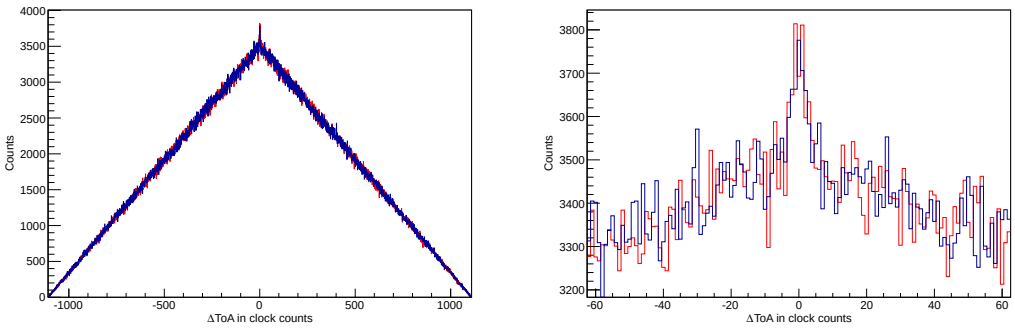

Figure C.3 Comparison of the simulated and measured spectra of the ToA differences. The full spectra can be seen in the left plot, a zoom into the region of interest is shown on the right. The red curves are simulation output.

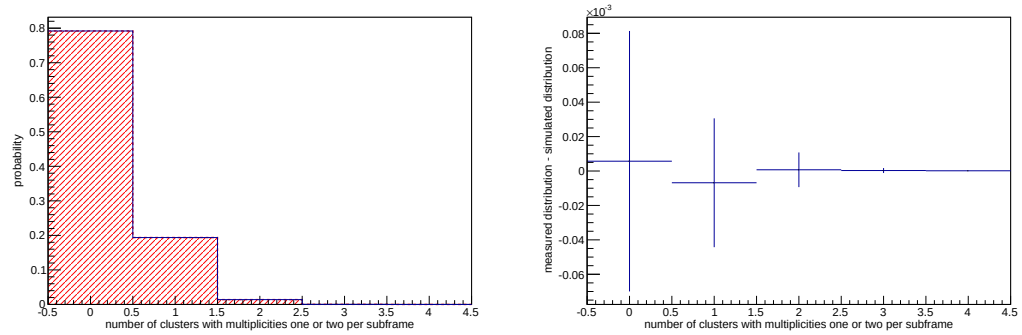

Figure C.4 Simulated (red) and measured (blue) distributions for the number of clusters with multiplicities one or two in one subframe (left plot) and the difference of these distributions (right plot) for measurement with the Kapton foil.

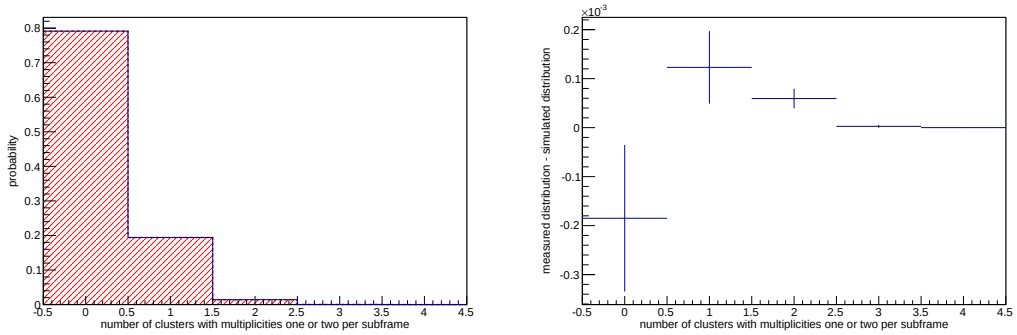

Figure C.5 Simulated (red) and measured (blue) distributions for the number of clusters with multiplicities one or two in one subframe (left plot) and the difference of these distributions (right plot) for measurement without the Kapton foil.

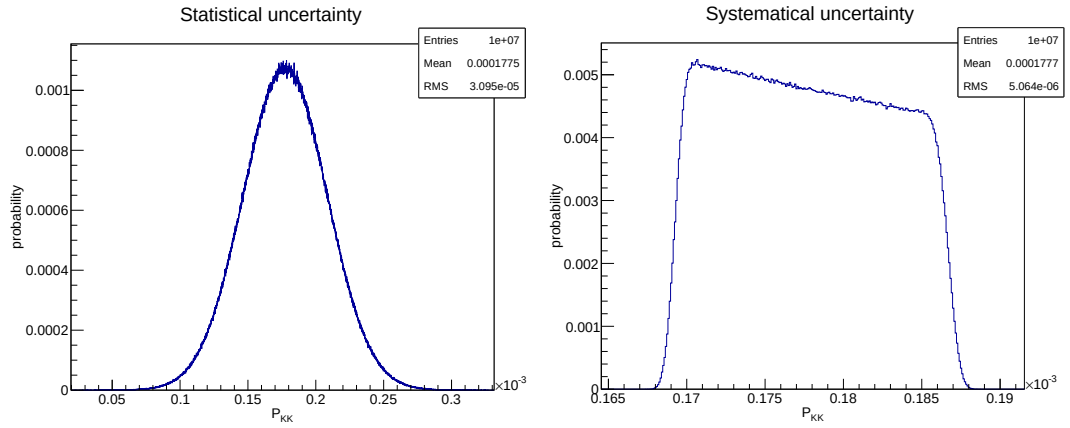

Figure C.6 Distribution of the P_{KK}-values taking into account the statistical errors (left) and the systematical ones (right).

D Plots of the P_{KK}-evaluation for H09W15

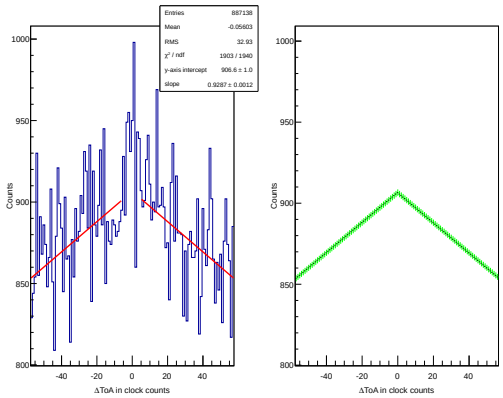

Figure D.1 Spectrum of time differences without the foil with the fit to the background on the left and extrapolation of the fit on the right. The detector is H09W15.

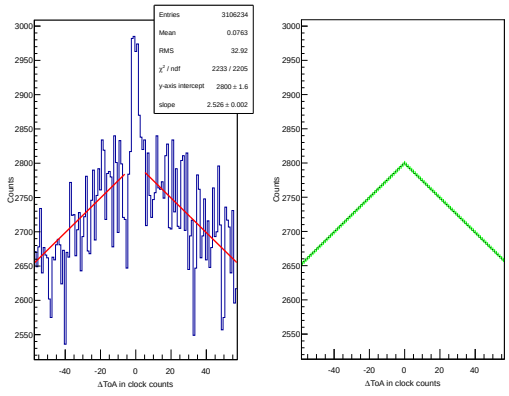

Figure D.2 Spectrum of time differences with the foil with the fit to the background on the left and extrapolation of the fit on the right. The detector is H09W15.

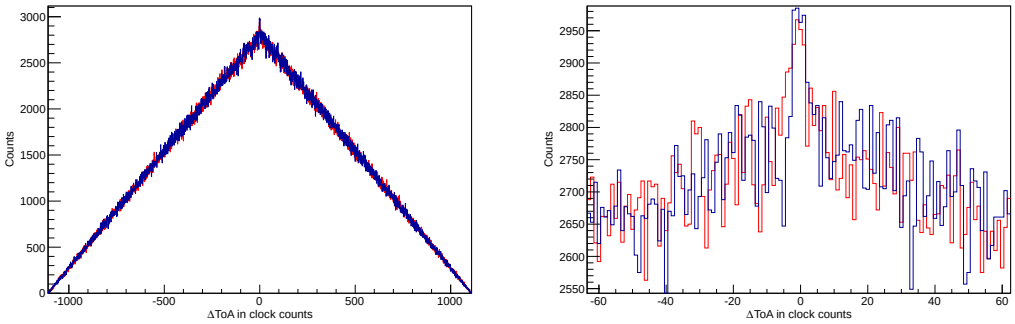

Figure D.3 Comparison of the simulated and measured spectra of the ToA differences. The full spectra can be seen in the left plot, a zoom into the region of interest is shown on the right. The red curves are simulation output.

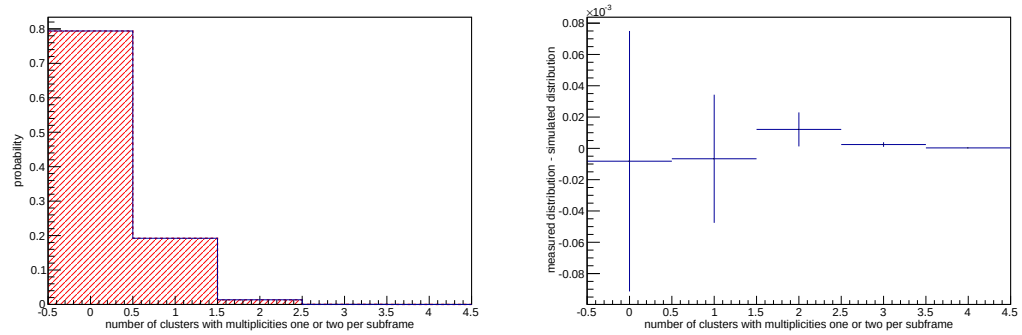

Figure D.4 Simulated (red) and measured (blue) distributions for the number of clusters with multiplicities one or two in one subframe (left plot) and the difference of these distributions (right plot) for measurement with the Kapton foil.

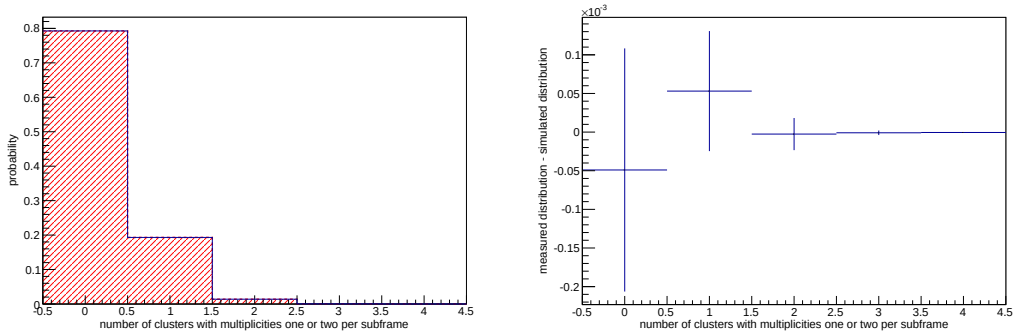

Figure D.5 Simulated (red) and measured (blue) distributions for the number of clusters with multiplicities one or two in one subframe (left plot) and the difference of these distributions (right plot) for measurement without the Kapton foil.

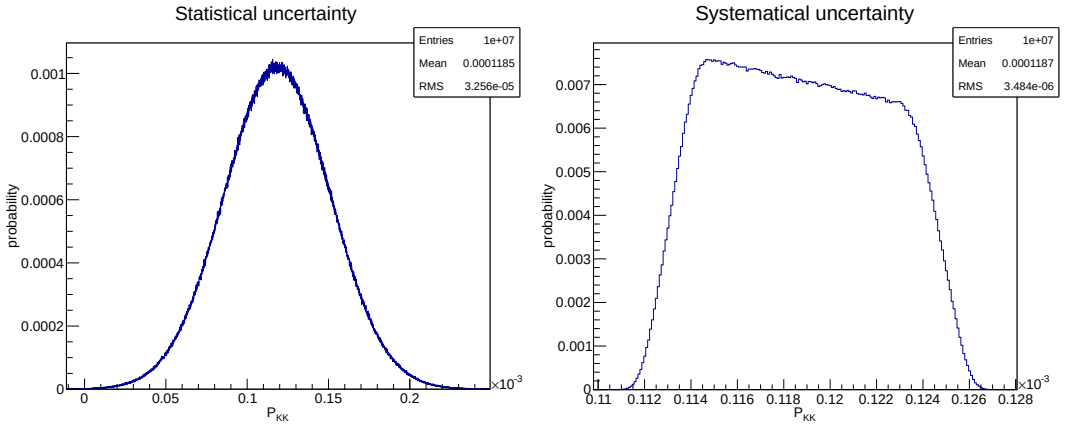

Figure D.6 Distribution of the P_{KK}-values taking into account the statistical errors (left) and the systematical ones (right).

List of Figures

List of Tables

Bibliography

[1] E. P. Kanter, I. Ahmad, R. W. Dunford, D. S. Gemmell, B. Krässig, S. H. Southworth, and L. Young. Double K-shell photoionization of silver. *Phys. Rev. A*, 73:022708, Feb 2006.

[2] D. Mitra, M. Sarkar, D. Bhattacharya, and L. Natarajan. Satellites, hypersatellites and RAE from Ti, V, Cr, Mn and Fe in photoionisation. *X-Ray Spectrometry*, 37(6):585–594, 2008.

[3] C.-C. Kao R. Diamant R. Sharon S. Huotari, K. Hämäläinen and M. Deutsch. Resolving the Mysteries of a Hollow Atom. *NSLS Activity Report*, 2001.

[4] J.P Briand, P Chevalier, A Johnson, J.P Rozet, M Tavernier, and A Touati. Experimental determination of the energy of K hypersatellite lines for various elements. *Physics Letters A*, 49(1):51 – 53, 1974.

[5] J. L. Campbell, J. A. Maxwell, and W. J. Teesdale. Double K-shell ionization in the electron capture decay of ^{55}Fe. *Phys. Rev. C*, 43:1656–1663, Apr 1991.

[6] http://www.nucleide.org/ddep_wg/nuclides/fe-55_tables.pdf.

[7] M. Filipenko. *Experimental Investigation of Pixelated Semiconductor Photodetectors with CdTe Sensor Material for the Search for the Neutrinoless Double Beta Decay.* master thesis, Friedrich-Alexander University, Erlangen, 2011.

[8] Xavi Llopart. *Design and characterization of 64k pixels chops working in single photon processing mode.* PhD thesis, Mid Sweden University, 2007.

[9] U. Gebert. *Untersuchung von Eigenschaften photonenzählender pixelierter Halbleiterdetektoren der Medipix-Familie.* Diploma thesis, Friedrich-Alexander University, Erlangen, 2007.

[10] T. Rügheimer. *Konzept und Eigenschaften eines Hybriden Photonendetektors auf Basis des Timepix-Detektors.* PhD thesis, Friedrich-Alexander University, Erlangen, 2009.

[11] J. Durst. *Modellierung und Simulation physikalischer Eigenschaften photonenzählender Röntgenpixeldetektoren für die Bildgebung.* PhD thesis, Friedrich-Alexander University, Erlangen, 2008.

[12] A. Korn. *Spektrale und bildgebende Eigenschaften photonenzählender Röntgendetektoren am Beispiel des Medipix-Detektors.* PhD thesis, Friedrich-Alexander University, Erlangen, 2007.

[13] http://aladdin.utef.cvut.cz/ofat/others/fitpix/fitpix.html.

[14] http://aladdin.utef.cvut.cz/ofat/others/pixelman/index.html.

[15] http://www.pi4.physik.uni-erlangen.de/giersch/rosi/index.html.

[16] J. G. Pengra and B. Crasemann. Energy Spectrum of Atomic Electrons Ejected in Electron-Capture Decay of Fe^{55}. *Phys. Rev.*, 131:2642–2648, Sep 1963.

[17] M. H. Biavati, S. J. Nassiff, and C. S. Wu. Internal Bremsstrahlung Spectrum Accompanying 1s Electron Capture in Decay of Fe^{55}, Cs^{131}, and Tl^{204}. *Phys. Rev.*, 125:1364–1372, Feb 1962.

[18] F. Lück. *Konzeption eines Experiments zum Nachweis des doppelten Elektroneneinfang-Zerfalls mit dem bildgebenden Röntgendetektor Timepix in Simulation und Messung.* Diploma thesis, Friedrich-Alexander University, Erlangen, 2007.

[19] http://root.cern.ch.

[20] Richard B. Firestone. *Table of Isotopes*, volume 1. John Wiley Sons, Ltd., New York, 1996.

[21] http://www2.dupont.com/kapton/en_us/assets/downloads/pdf/hn_datasheet.pdf.

[22] http://www.astm.org/standards/d1505.htm.

[23] http://www.autoitscript.com/site/autoit.

Acknowledgements

I would like to thank the following groups and people for supporting me and my work on this thesis:

- All members of the **Radphys group** for the great atmosphere, the interesting team meetings, the inspiring days in Bärnfels, the nice coffee breaks and all the other activities not mentioned.
- **Michael Böhnel** for being able to answer all my question on the Timepix devices, yielding his well calibrated Timepix device to me and organizing the weekly football practice.
- **Florian Bayer** for the rehearsals in Baiersdorf.
- **Thomas Gleixner** and **Mykhaylo Filipenko** for always finding the causes for the segmentation faults I produced.
- **Wilhelm Haas** for coping with all Pixelman problems and the great discussions about politics.
- **Peter Sievers** and **Thomas Weber** for giving usefull hints and advice on the LaTeX package.
- **Jutta Dziwis** for the help with all the administrative stuff concerning my business trips and work contract.
- **Jürgen Durst** for the ROSI and HPC introduction, fixing my ROSI coding mistakes and all the suggestions and discussions about my data evaluation.
- **Gisela Anton** for the possibility to write this thesis in the Radphys group.
- **Thilo Michel** for his great way of motivating people, his great ideas and suggestions, for finding peaks in spectra where I would never have seen anything ;), showing me how to use Pixelman and to perform THL-Scans, helping me setting up the trigger electronics, and much more.

Last but not least, a special thanks to all my roommates during the time of this thesis, that had to stand me nearly every day, my family and friends and all persons I forgot to mention.

Declaration

I declare that I have authored this thesis independently, that I have not used other than the declared sources, and that I have explicitly marked all material which has been quoted either literally or by content from the used sources.

Erlangen, 10th September 2012

Benedikt Bergmann